Journal of Applied Geophysics 195 (2021) 104497

Contents lists available at ScienceDirect

Journal of Applied Geophysics

journal homepage: www.elsevier.com/locate/jappgeo

Geoelectrical properties of saline permafrost soil in the Adventdalen valley of Svalbard (Norway), constrained with in-situ well data

Saman Tavakoli [a,*], Graham Gilbert [a,b], Asgeir Olaf Kydland Lysdahl [a], Regula Frauenfelder [a], Cathinka Schaanning Forsberg [c]

[a] Department of Natural Hazards, Norwegian Geotechnical Institute, 3930 Ullevaal Stadion, Oslo N-0806, Norway
[b] University Centre in Svalbard, UNIS, Arctic Geology Department, Longyearbyen, P.O. Box 156, Norway.
[c] Department of Offshore Energy, Norwegian Geotechnical Institute, 3930 Ullevaal Stadion, Oslo N-0806, Norway

ARTICLE INFO

Keywords:
Sedimentary deposits
DC resistivity and induced polarization
2D inversion
Svalbard
Geotechnical engineering

ABSTRACT

Direct Current (DC) Resistivity and Induced Polarization (IP) response of six profiles were measured using the Gradient electrode configuration in Adventdalen, Svalbard, to characterise the near-surface stratigraphy of the soil and to account for geotechnical and environmental aspects of global warming in the arctic region. In addition, Wenner array data was collected for the selected profiles to examine its effectiveness as compared to the Gradient array, given the characteristics of the study site. Two commercial inversion software programs, Res2DINV and AarhusINV, were used for the inversion of the DC resistivity and IP data, to compare the software. Physical soil properties, including porosity, water saturation, water salinity, freezing temperature and grain size distribution, previously measured from samples retrieved from wells along the studied profiles, were integrated in this study to investigate the correlation with geoelectrical properties of the sediments inferred from the DC resistivity and IP data.

Results from processing of the Wenner array DC resistivity data provided higher resolution as compared to the Gradient array data, especially from deeper parts of the models, due to its higher signal-to-noise ratio. The Wenner array data also indicated better inversion result for the IP data as distinctive anomalies were better indicated in data from Wenner array survey. The Wenner array data also provided a realistic trend for the anomalies, thanks to the symmetrical geometry of the electrodes during the survey, although at the cost of time and higher expenses. Inversion results proved that AarhusINV resolved the geometry of the subsurface layers with higher resolution compared with the Res2DINV. However, the two inversion algorithms use slightly different parameters for the processing and for presenting the results, thus only allowing qualitative comparison. Based on the interpretations of the DC resistivity and IP data, four distinctive zones were identified from the surface to the maximum depth of 26 m, consisting of (i) unfrozen active-layer-(silts and sands), with intermediate resistivity values 200–300 Ω·m; (ii) frozen soil with 3–10 m thickness and resistivity values between 2500 and 5000 Ω·m; (iii) unfrozen soil (cryopeg) with high salinity and low resistivity of 40 Ω·m; and finally (iv) clayey-unfrozen soil sediments with low resistivity ranging 10–20 Ω·m, at depths between 13 and 26 m. The IP data allowed for the delineation of a low chargeability zone near the surface and a high chargeability zone at greater depth which denote the active layer, lower parts of unfrozen soil sediments and cryopeg respectively, within the top 10 m of the subsurface.

The 3D subsurface model of the study area was created based on interpretations of the DC resistivity and IP data and was constrained by the description of the subsurface stratigraphy from nearby wells, which provided detailed information about the vertical stratigraphy of the study area. In addition, a good correlation was observed between the studied physical properties of the sediments and the DC resistivity data for the intersecting profile SVAER04, as the interface between high and low resistivity data at ca. 10 m depth coincided the sedimentary formation with intermediate-fine grain size, high porosity, high water saturation and high salt content. Our findings show that joint application of the geoelectrical surveys and laboratory analysis of soil samples are an efficient complement to each other. These methods can be used as an alternative to each other to investigate larger areas where achieving high resolution data is not necessary.

* Corresponding author.
E-mail address: Saman.tavakoli@ngi.no (S. Tavakoli).

https://doi.org/10.1016/j.jappgeo.2021.104497
Received 1 May 2021; Received in revised form 14 September 2021; Accepted 2 November 2021
Available online 5 November 2021

Our study results underline the importance of choosing the right survey design for collecting the DC resistivity and IP data. Contribution of the IP data in this study mostly concerns the shallow parts of the subsurface due to the low signal-to-noise ratio at greater depths, and frozen ground which limited the ion mobility and hence the IP response. An appropriate inversion program coupled with integration of the physical properties of the sediments, can be successfully applied to characterise the near-surface morphology of the sedimentary formations to address the geotechnical and environmental challenges related to the permafrost in the Arctic.

1. Introduction

1.1. Motivation

Global warming affects the Arctic faster than any other region on Earth, with temperature increases double the global average (e.g., Mcbean et al., 2005). Since 1980s, temperature at the top of Arctic permafrost layers has increased by up to 3 °C (Lemke et al., 2007). In Adventdalen, increasing temperatures led to an increase in the thickness of the seasonally-unfrozen active layer in sediments by 0.6 cm per year since the year 2000 (Christiansen et al., 2019; Hanssen-Bauer et al., 2019). A thickening active layer leads to increased penetration of heat into the ground, which subsequently leads to warming and, ultimately, thawing of permafrost. Thawing permafrost releases greenhouse gases, including carbon dioxide and methane, causing a considerable negative impact on global warming, and leading to damage the natural hydrological cycles such as water drainage. Understanding the stratigraphy of the permafrost and its sedimentary layers with the ice and salt contents is fundamental to better understand (i) the risk associated with land subsidence due to the thaw effects of the permafrost, (ii) the impact of permafrost thawing on the emissions of greenhouse gases, and (iii) the ecosystem of the permafrost and to monitor its temporal variations.

Studies indicate that variations in the amount of unfrozen water content caused by either seasonal changes, climate change, and infrastructure development, or a combination of these, results in e.g. a thickening of the active layer (Arenson et al., 2007; de Grandpré et al., 2012). The degree to which the thickness of the active layer increases depends also on the excess-ice content (Gilbert et al., 2018). According to Gilbert et al. (2019) the concentration of pore water solutes facilitates the presence of cryopegs (zones of unfrozen cryotic soil which remain unfrozen due to the presence of salts in the pore water) which complicates geotechnical conditions as pore water salinity influences the freezing temperature and mechanical behaviour of the soils.

The subsurface can be characterised accurately by e.g. drilling, core samples analysis and well-logging. However, such direct methods are costly and provide information from a local perspective only. Characteristics of the subsurface, such as the depth of the frozen-unfrozen ground interface, active layer delineation and occurrence/absence of cryopeg zones can be efficiently studied at low cost, in large scale and within short time by using of geophysics, including Direct Current Resistivity (DC) and Induced Polarization (IP) methods (hereafter abbreviated as DCIP where both methods are meant).

This study aims to image the vertical and lateral distribution of the near-surface stratigraphy with DCIP data, down to approximately 20–40 m depth.

More specifically, the following challenges related to permafrost properties are addressed in this study using the DCIP data and the physical parameters of the sediments:

I. Determining the thickness of the active layer of the permafrost in Adventdalen;
II. Identify and characterise the overpressure cryopeg within the saline permafrost soil;
III. Study of the correlation between physical properties of the sediments including water salinity, porosity, freezing point temperature, water saturation and sample's grain size (from borehole wells A3 to A5), and information retrieved from the DCIP profiles identifying the cryopeg zone;
IV. Validation of the effective application of high resolution DCIP data to create a 3D subsurface model of the permafrost.

In addition, we aim to investigate the following technical geophysical aspects:

- Optimal choice of the electrode configuration given the geological setting of the study site within the shallow-subsurface arctic environment in Adventdalen, Svalbard;
- Effectiveness of using the IP method to investigate the permafrost in the Arctic;
- Comparison between results from different inversion algorithms and their impact on the results.

1.2. Earlier studies on the geoelectrical properties of the permafrost

The electrical resistivity of sediments and rocks is a function of several parameters including porosity, water content, pore-water ion concentration and sample's grain size (Tavakoli et al., 2012). Freezing of the rock's water content increases the electrical resistivity by transforming the electrical conductor “water” into the insulator “ice” (Doetsch et al., 2015). Due to other factors influencing the DC resistivity, the inverted resistivity data cannot be transformed directly into temperature, especially when changes in water saturation might happen simultaneously to freezing (Doetsch et al., 2015). Moreover, high porosity and high groundwater conductivity reduce the IP effect, since both parameters lead to a short circuiting of the energising current through unblocked paths (Parasnis, 1979). Results from IP measurement are sensitive to the ratio of the grain surface to pore volume and the grain surface charges (Lesmes and Frye, 2001; Slater and Lesmes, 2002). Changes in the electrical properties of the subsurface porous media can be used to estimate unfrozen water content in the frozen soil (e.g. King et al., 1988; Fortier et al., 1994). Hauck (2002) and Hauck et al. (2008) successfully used DC resistivity and borehole temperature data to monitor the temporal variation of the unfrozen water content at a high-alpine permafrost site in the Swiss Alps. Oldenborger and LeBlanc (2015) studied the continuous changes of the unfrozen water content using DC resistivity surveys in the permafrost at the Iqaluit International Airport (Nunavut, Canada) to address deformations attributed to active-layer thickening and permafrost degradation, which had resulted in severe geotechnical problems. In another study, near-surface conditions of two types of patterned ground, ice-wedge polygons and mudboils was continuously monitored in Svalbard using the DC resistivity data (Watanabe et al., 2012). Hauck et al. (2008) developed an approach to characterise subsurface ice, water, and air contents in permafrost regions using a 4-phase model by studying the petrophysical, electric and elastic properties of the material. The 4-phase model approach helped to delineate the internal layers including the active layer which was indicated by strong contrasts between studied properties of vertical ice and air content distribution. In Svalbard, Hornum et al. (2021) studied the water flow through permafrost in lower Adventdalen using the DC resistivity data. The considerable contrast between the resistivity response of the uphill and valley-sides of the pingo was explained as boundary between low-permeable marine sediments and consolidated strata. Their study suggests that the groundwater flows towards the pingo

spring through the fractures in the strata which underlines the marine sediments.

1.3. The cryopegs

The presence of unfrozen, cryotic zones within permafrost is well known in the Longyearbyen area (see e.g. Keating et al., 2018). Redistribution of salts present in the soil's pore water creates pockets of unfrozen cryotic brine in the permafrost soils. The salt concentration lowers the freezing point of the soils considerably to a temperature as low as e.g. -6 °C. Soils which are comprised of marine sediments contain residual salts from the time of deposition which are redistributed through pore-water expulsion during the permafrost growth. Salt concentrations at geological barriers form pockets of hypersaline soil (salinity up to ca. 7%), which can remain unfrozen even at temperatures between −4 °C to −6 °C (Gilbert et al., 2019). Cryopegs are normally under high pressure due to the forces generated during freezing and the stress imposed by the overlying soil. The size of these pockets expands and modifies with variations in the soil temperature. With climate change, permafrost soil temperatures are rising which results in increase in prevalence and size of cryopegs. Drilling reports from Longyearbyen confirm the presence of unfrozen soil sediments and liquid water within the permafrost, and cryopegs were recently identified between 15 and 20 m depth during field investigations in Adventdalen (Gilbert et al., 2019). Understanding the spatial distribution of these features not only is important to study the global warming effects in the Arctic, it also helps to reduce the challenges and potential hazards which maybe be experienced during e.g. geotechnical engineering projects.

1.4. Context of the field site

The field site used in our study belongs to a network of five Norwegian Geo-Test Sites (NGTS) that were established between 2016 and 2018. While four of the sites are established in western and south-central Norway, one is established in the Adventdalen, at the site described below (Fig. 1).

During the past years, several borehole wells were drilled at the site. Five sampling methods were used to provide material from different sedimentary layers from the wells A3 to A5 (Fig. 1) for in-situ laboratory experiments. These methods included total sounding, drilling with conventional auger, core sampling using CRREL, piston sampling and Down The Hole (DTH) drill. The sampling from active layer was conducted using the auger drilling and sampling of the permafrost was mainly performed using the CRREL coring auger with 54 mm piston sampler and steel cylinders. At further depths, where the condition was challenging e.g. below the thick cryopeg, the sampling was performed using the auger method. Additional details about the drilling process is provided by Gilbert et al. (2019). Classification tests have been performed in the laboratory to characterise the samples from the wells A3, A4 and A5 and down to ca. 30 m depth in Adventdalen (Gilbert et al.,

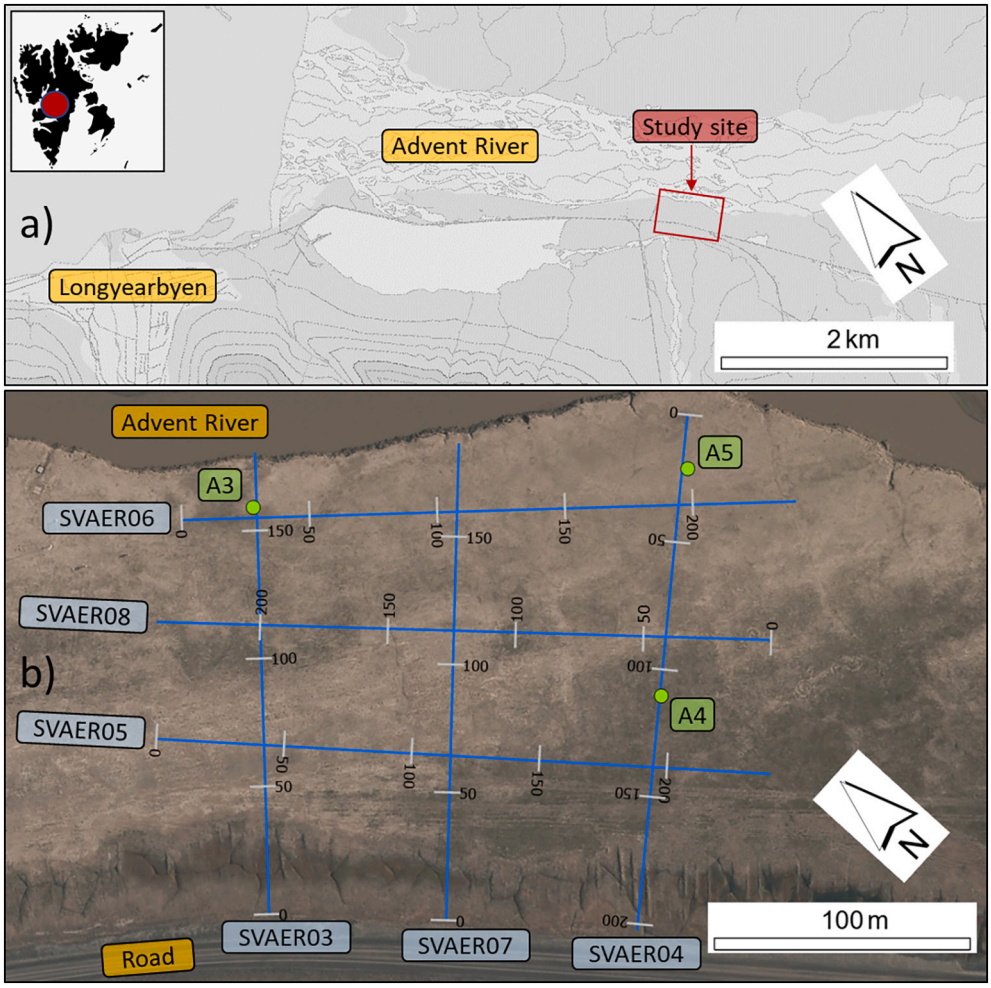

Fig. 1. a) Study area in Adventdalen (red circle) and site location (red rectangle). b) Location of the DCIP profiles SVAER03–SVAER08 and the borehole wells with incorporated petrophysical data from the NGTS site are marked by green, labelled (A3 to A5) circles. (For interpretation of the references to colour in this figure legend, the reader is referred to the web version of this article.)

2019).

Gilbert et al. (2018) studied the stratigraphy and soil conditions in Adventdalen from drilling cores at the site where the DC resistivity fieldwork took place. Three soil units were described within the top 30 m of the sub-surface as three major units D1, D2 and D3. Unit D1 was explained as a 3 m thick top layer of sandy and clayey-silt, representing loess deposits. The underlying Unit D2 is described as a 13 m thick and contains interlayered graded sands and silts, representing delta slope deposits. Unit D3, can be found between 16 m and 30 m depths and is consist of laminated or weakly laminated muds, representing delta-foot deposits.

In our study, the following physical properties of the sediments were incorporated to the interpretations to account for their potential relationship with the electrical properties from interpretations of the DCIP data: water saturation, sample porosity, water salinity, freezing depression point and sample's grain size.

2. Geomorphology of the study area

Svalbard was glaciated several times in the late Quaternary (Mangerud et al., 1998; Ingólfsson and Landvik, 2013). The last glacial maximum culminated around 20 ka BP, and Svalbard and the Barents Shelf were covered by a thick ice-sheet (Landvik et al., 2005). Adventdalen (Fig. 1) is a fjord-valley and a side tributary to the much larger geomorphic system of Isjorden that drained Svalbard ice to the shelf edge during the late Weichselian glaciation (Ingólfsson and Landvik, 2013). Adventdalen was shaped as the ice carved in flat-lying Early Cretaceous and Paleogene sedimentary rocks consisting of mainly sandstones and shales (Major et al., 2001). Most of the sedimentary record of previous glaciation-deglaciation cycles were removed in fjords and valleys when the ice advanced (Elverhøi et al., 1995), and a layer of over-consolidated subglacial till was formed (Forwick and Vorren, 2009).

Deglaciation commenced at ca. 15 ka (Landvik et al., 1998), and by ca. 10 ka, Adventdalen was ice-free (Svendsen and Mangerud, 1997; Lønne and Lysså, 2005). The sea level at this time was ca. 62–70 m higher than present level in the study region (Lønne, 2005), and muddy glaciomarine sediments were deposited in a deglaciated fjord (Gilbert et al., 2018). The rates of glacio-isostatic crustal rebound outpaced the eustatic sea-level rise accompanying the deglaciation, resulting in a forced regression in Svalbard (Gilbert et al., 2018). A delta system prograded from the fjord-head, resulting in younger Holocene deltaic deposits covering the previously deposited muddy glaciomarine sediments (Gilbert et al., 2018). The relative sea level was declining during the Holocene and reached its current level at ca. 5 ka BP (Lønne and Nemec, 2004).

The forced regression led to the incision of rivers feeding the delta system, leaving behind raised alluvial terraces at the fjord-valley margins subject to aeolian sedimentation since ca. 3 ka. The gradual subaerial exposure of the fjord-fill allowed for permafrost aggradation with an onset of the development expected to decrease in age in a down-fjord direction. Both syngenetic and epigenetic permafrost have been identified in Adventdalen. Syngenetic permafrost grows upwards during deposition of additional sediment and occurred in Adventdalen with the accumulation of loess deposits on the alluvial terraces. The underlying zone of epigenetic permafrost formed by downward freezing of the fjord-fill sediments and their exposure to low subaerial temperatures (Gilbert et al., 2018).

3. Geophysical field work

The DCIP data were collected along six profiles in Adventdalen (Fig. 1), three of which oriented NE-SW (SVAER03, SVAER04 and SVAER07) and three others in NW-SE direction (SVAER05, SVAER06 and SVAER08), with profile lengths being between 176 and 240 m. All profiles were measured using the Gradient array. In addition, two of these profiles (profiles SVAER05 and SVAER06; Fig. 1) were also measured using the Wenner array. In the Wenner array, only the response from centre potential dipole is measured, whereas the Gradient array measures the response from all adjacent dipoles from one transmitter electrode to the other. Compared to the Wenner array, the Gradient array is expected to provide a stronger signal near the two current electrodes, but a weaker signal at the centre of the survey area (see e.g. Dahlin and Zhou, 2004; Cyril, 2013).

The fieldwork was carried out in late September 2020 when the air temperature was around 0 °C. By then, a thin layer of snow covered the top soil. However, except for the uppermost centimetres of soil towards the end of the survey period, the underlying active layer was unfrozen throughout the entire survey. An ABEM LS2 Terrameter was used for data acquisition with a spread of 4 × 21 electrodes. The electrode spacing was varied for different profiles to make it compatible with the expected ground conditions (Table 1). The Gradient XL electrode configuration with the 100% IP duty cycle was used to measure the IP response of all profiles. No major problems were encountered during installation of the electrodes into the ground. Ground resistance threshold was set to 5000 Ω. The maximum allowed injection voltage and maximum power used were 400 Volts and 150 W, respectively.

The multi-channel Gradient array which is capable to make several measurements simultaneously, was served as the main electrode configuration during the field work. The potential electrode pairs at different locations were moved in between the current electrodes which were placed at fixed locations. The high speed for data acquisition and expected high-data density was the main motivation for conducting the field work using the Gradient array. This, however, at the cost of somewhat lower signal-to-noise (S/N) ratio and poor resolution at deeper parts compared to the Wenner array. The Wenner array was used in addition to the Gradient array, to measure the DCIP data along the profiles SVAER05 and SVAER06 to compare the effectiveness of the two arrays given the survey environment (Fig. 1). The Wenner array was preferred to be used alongside the Gradient array due to (i) the high S/N ratio and, therefore, high resolution to resolve structures from deeper parts, and (ii) its effectiveness in imaging vertical resistivity variations of the subsurface. The downside of the Wenner array is its relatively poor ability to image horizontal variations of the subsurface resistivity (see e.g. Loke, 2011), which is, however, not a dominant attribute in the stratigraphy of the shallow subsurface in Adventdalen. Theoretically, the survey design was expected to image the apparent resistivity down to ca. 40 m depth. The study area offers an open environment free from man-made structures within a radius of >200 m. The general rule is to avoid high-voltage power lines and other likely sources of the electromagnetic (EM) noise by considering a distance twice as large as the desired penetration depth. Therefore, the likelihood for EM disturbance affecting the DCIP data was minor. The IP data were measured in the time-domain (TDIP) in millisecond (ms), by measuring the decay of the electric potential after the transmitter current is switched off. The IP effect originates from one of two sources: (i) electrode polarization (electronic source), mainly in the case of metallic minerals, or (ii) membrane polarization (ionic source), mainly in the case of clay minerals. The IP method is especially effective where disseminated or semi-disseminated concentration of materials is to be detected (Tavakoli et al., 2012). In this study and due to the presence of the clayey sands,

Table 1
Field characteristics of the DCIP geophysical profiles.

Profile	Length (m)	Electrode spacing (m)	Electrode array type
SVAER03	176	2	Gradient XL
SVAER04	200	2.5	Gradient XL
SVAER05	240	3	Wenner, Gradient XL
SVAER06	240	3	Wenner, Gradient XL
SVAER07	186	2	Gradient XL
SVAER08	240	3	Gradient XL

the cause for an IP effect, if any, was expected to be membrane polarization within the unfrozen soil sediments. During measurements, the acquisition period was set to 2.0 s and the delay time to 0.01 s. The period was divided into ten integration windows (Table 2).

4. Modelling scheme

Inversion of the DCIP data was performed using the two inversion programs Res2DINV (Loke, 2011) and AarhusINV (Auken et al., 2015; Aarhus Workbench, 2021). The inverted DCIP sections were thereafter georeferenced and integrated into the modelling and visualization platform Leapfrog work 4.0 © (hereafter abbreviated as Leapfrog). In addition, description of the sedimentary stratigraphy and physical parameters from the borehole wells (including porosity, water salinity, water saturation, sample's grain size and freezing temperature point) were integrated into Leapfrog to create property models and for integrated interpretations. High resolution elevation data with 5 cm resolution were also imported as a GeoTIFF file to Leapfrog.

Each inverted 2D profile was studied separately for detailed interpretations of the DCIP anomalies. 3D modelling was performed in Leapfrog by interpolation of the following properties: (i) description of the sedimentary deposits calibrated to well data, (ii) interpretations based on 3D integration of the DC resistivity, and (iii) of IP data. The two latter datasets served as a basis to create the main interpretations, that is, the sliced depth models and modelled cross-sections. The following considerations must be accounted for prior to the selection of an appropriate surface resolution for creating 3D models in Leapfrog: (i) the purpose of the model, (ii) the length of the shortest interval that the model is based on, and (iii) the complexity of the subsurface geology. In this work, adaptive surface resolution was selected, which is appropriate for datasets with intensive variations for the spacing between e.g. polylines or drill-holes. This way, the program is enabled to accurately model the areas with high data density while maintaining appropriate resolution for parts of the model where data density is relatively low. As a result, the generated triangles constituting the surface closer to the polylines were smaller compared to those located further away, which can explain the blank volumes at parts of the models since the resolution was low (coarse cells) to create a surface from the narrow interval surfaces.

The 3D resistivity model was created using a five-layered scenario with 20 m surface resolution. However, adaptive resolution was allowed. For the IP model, since the intensity in variation of the IP anomaly was less compared to the resistivity data, a 40 m surface resolution was selected. In addition, the slice depth models and modelled cross-sections were retrieved from the generated 3D model for detailed interpretations (Fig. 2).

The subsurface model stratigraphy was created based on 3D integration of the DCIP data and interpretations was constrained by physical parameters from the wells which explains the general sedimentary layout of the subsurface down to 26 m depth at the study site in Adventdalen.

Table 2
Integration windows and the corresponding time windows during the IP data survey.

Integration window	Measurement time (s)
1	0.06
2	0.06
3	0.12
4	0.12
5	0.12
6	0.18
7	0.24
8	0.30
9	0.36
10	0.42

5. Results

5.1. Correlation between DCIP data and physical parameters of the sediments

The relationship between electrical properties of soils and sediments and their physical parameters can be explained by Archie's law. This law states that the electrical properties are a product of the electrical conductivity of the porous media and brine, the bulk porosity of the rocks, the cementation factor (which again depends on grain shape and type), the clay content, and the degree to which sediments are mixed (Tavakoli et al., 2012).

Differences in physical properties of the sediments such as grain size, porosity, water salinity, water saturation and the freezing temperature, influences the measured resistivity and chargeability response of the subsurface sediments. These parameters affect the form of the current-flow through the soils and sediments, resulting in variations in the distribution of the electric potential within them (Ebiegberi and Isaac Oludayo, 2021). Although these parameters are provided from in-situ laboratory experiments on samples in a micro-scale, they can be studied to understand their effects in macro-scale by studying their correlation to the DCIP data acquired from geoelectrical surveys. The petrophysical parameters measured on sediments of the NGTS site in Adventdalen and their expected resistivity and chargeability response is briefly explained below.

5.1.1. Sample's grain size

The electrical resistivity of sediments tends to increase as particle size increases, provided that other physical parameters remain unchanged. Clays in general demonstrate lower resistivities compared to coarse grained sands, which can be explained by the pronounced current conduction through electrolytic and electronic conduction in clays (Ebiegberi and Isaac Oludayo, 2021). Small differences in particle size, e.g. ≤ 5 times may be uncapable to be detected in the results from in-situ resistivity measurement of the samples (Erchul, 1972). In this study, the soil sediments were classified based on their grain size as gravel, sand, silt and clay, from coarse to fine grains respectively (Gilbert et al., 2019; Table 3). In general, the deeper parts of the stratigraphy observed in the borehole samples are constituted of higher amounts of fine grain clay content as compared to the upper parts, which comprise greater portions of coarse grain sediments, i.e. sand and gravels (Fig. 3a).

5.1.2. Water saturation, salinity, sample's porosity and Soil sediments freezing point depression

5.1.2.1. Water saturation. The electrical resistivity of the soil sediments depends also on the amount and electrical conductivity of the pore water. This effect can be observed on the electrical resistivity of dry sands which is about 10^4 times higher compared to saturated sands (Fukue et al., 1999; Muñoz-Castelblanco et al., 2012). As a result, if porosity and water saturation increase simultaneously, the electrical resistivity decreases (Erchul, 1972). In this study, sample water saturation is highest at depths between 5 and 15 m for wells A4 and A5 and tends to decrease at greater depths (Fig. 3b). Since wells A4 and A5 are located in the vicinity of the profile SVAER04, the correlation between water saturation and DC resistivity of the profile SVAER04 will be discussed in the chapter 6.

5.1.2.2. Water salinity. The influence of clay minerals on the resistivity of the subsurface material is greatly dependent on the type of the predominant clay minerals and the salinity of the pore water. As clays get in contact with an electrolyte, the negative charges on the clay surface attract positive ions and repulse negative ions present in the electrolyte solution. This generates an electrical ionic double layer, a so-called “diffuse layer” on the outer surface of the particles (Takakura, 2009).

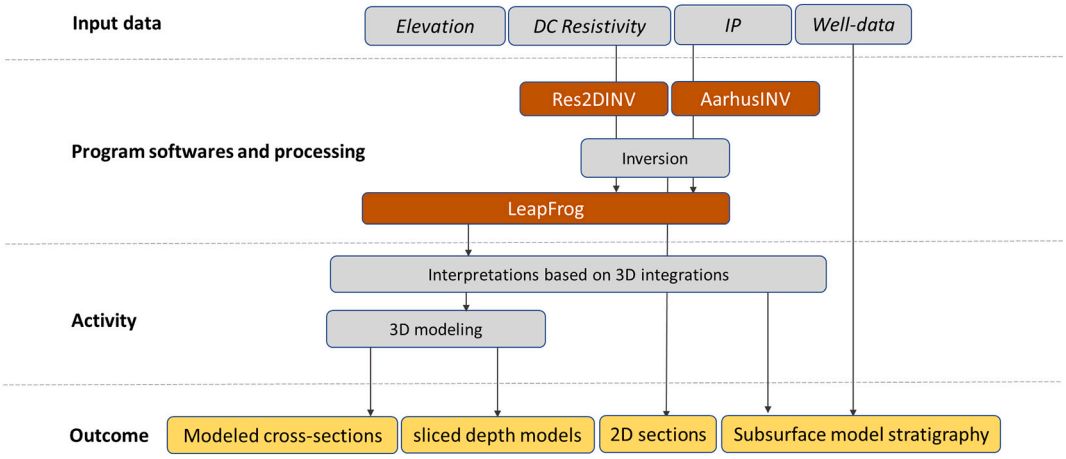

Fig. 2. The modelling and interpretation scheme including the input data, program softwares for processing, and interpretations, 3D modelling and interpretation activities and the model outcomes.

Table 3
Grain size distribution and types of the of the sediments from the NGTS study in Adventdalen, Svalbard modified after (Gilbert et al., 2019) for the wells A3 to A5. The sediment's grain size used for classifications and proportion percentage of each type of sediment is indicated.

Description	Classes of sediments based on grain size			
Type of the sediments	Gravel	Sand	Silt	Clay
Grain size ranges	63–2 mm	2–0.063 mm	63–2 μm	> 2 μm
Proportion of sediments based on grain size (%)	0.4	32.6	50	17

According to Denicol and Jing (1998), the salinity-dependence of the pore water relates to the thickness variations of the double layer and the ion mobility. Decrease in salt concentration increases the thickness of the diffuse layer (Denicol and Jing, 1998) which favours blockage of the ions, especially at narrowing pores which will be indicated by lower resistivity values. Water salinity of the pore water was measured on selected samples and was analysed using the ISO 11265 standard (Fig. 3b; Gilbert et al., 2019). Water salinities tend to increase with increasing depth, which according to Gilbert et al. (2019) is related to the salt re-distribution during permafrost growth. Maximum values of water salinity can be observed at depths between 10 and 20 m (Fig. 3b), which is expected to associate with low resistivities, provided that other physical parameters are the same.

5.1.2.3. Sample porosity. The main purpose of incorporating the porosity and water salinity measurements into this study was to understand the condition of the soil and the permafrost. Increased porosity associated with high water saturation and high water salinity is expected to demonstrate lower resistivity values (Lu et al., 2019). Sample porosities of the here discussed samples range mainly between 35 and 83%. However, at depths ≥10 m most of the samples indicate porosities between ca. 40–60% (Fig. 3b).

5.1.2.4. Soil freezing point depression. The soil freezing point is defined as the temperature at which the soil begins to freeze. For the samples discussed in this study, it was determined by placing a temperature probe into a thawed sample and thereafter putting the sample into a cold storage with -18 °C temperature (Gilbert et al., 2019). The highest freezing points (−4 °C to −5 °C) were recorded between 10 and 20 m depth, and the lowest values were observed below 5 m depth (Fig. 3c).

5.1.2.5. IP effects. The ability of clay minerals to hold charges is controlled by the surface interactions between clay minerals and fluids, which reflects on the IP response. Therefore, the IP properties of sediments depends greatly on their ability to accumulate ionic charges. The study results by Denicol and Jing (1998) indicate that the IP effects from partially saturated samples is higher than that of fully saturated samples. The IP effect also depends on the salinity of the pore water, i.e. the concentration of ions within the pore water. As the pore-water salinity increases, so does the capacity of the rock to support build-up of the ionic charges, which results in an increased chargeability in the rock. Both sources of the IP effect (membrane and electrode polarizations) are also related to grain size and material type. Therefore, discrimination of mineral type based on chargeability values is complicated and does not provide accurate results. Subsequently, correlations between the sediment's physical parameters and the IP response are excluded from this study.

5.2. Inversion of the DCIP data

All profiles were processed using two inversion programs Res2DINV (Loke, 2011) and AarhusINV (Auken et al., 2015; Aarhus Workbench, 2021). Various input parameters were tested during the inversion and although minor discrepancies could be observed in the results from the two inversion programs, the general distribution of the resistivity and chargeability data did not differ considerably. AarhusINV provided a smoother anomaly pattern with less inversion artefacts, which is expected given the stratigraphy of the study area. In addition, it resolved the features of interest with more details from the stratigraphy of the site compared to the Res2DINV particularly for the IP data. Therefore, final interpretations are merely based on the result from the AarhusINV. A brief description for the general settings and input inversion parameters is explained below.

Frequency domain IP (FDIP) data can either be measured as percentage frequency effect (PFE) or phase differences between the source and measured potentials recorded as a measure of the chargeability milliradians (mrad). In Time-Domain IP (TDIP), the integrated chargeability which is defined as the area under the discharge curve is normalized by the DC voltage and presented in milliseconds (ms). IP responses when measured and presented in different domains produce results presented in different units. Conversion between the TDIP and FDIP data can be calculated by Fourier transformations and is rather complicated. Nevertheless, using an approximate rule of thumb, one can estimate the chargeability value of M = 0.1 equal to 10 (PFE) = 70 (mrad) = 70 (ms). The results from the inversion of the IP data achieved from the two programs are presented in TDIP and are given in ms.

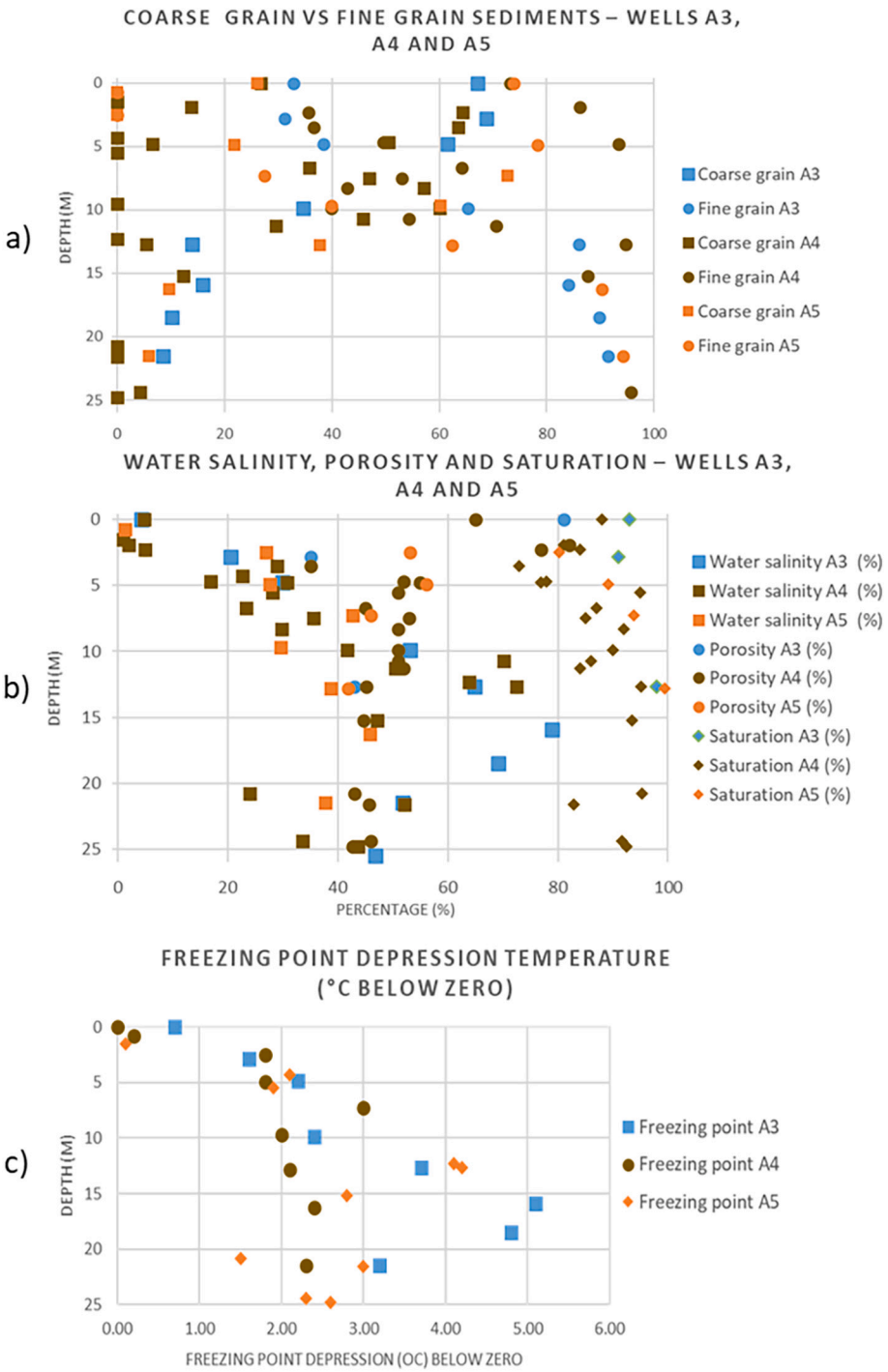

Fig. 3. Measured physical parameters of the wells in Adventdalen from the NGTS study. a) Coarse grains (gravel and sand) and fine grain (silt and clay) distribution for the wells A3 to A5, b) porosity, water saturation and water salinity for the wells A3 to A5, and c) freezing point temperature for the wells A3 to A5 (source of data in figure: Gilbert et al., 2019).

5.2.1. DCIP inversion in Res2DINV – Gradient array profiles

The DCIP response of the profiles SVAER03–SVAER08 was calculated using the Res2DINV Ver.4.10. Before running the inversion, we removed the "bad" data points or outliers from the datasets by applying a cut-off error limit when necessary. The inversion was performed in Res2DINV using the both the default parameters and a modified inversion. For the latter, adjustments of the inversion parameters were done, in order to evaluate if an improvement of the inversion result is achieved. In the default setting, we used standard data and model constraint (L2) with a cut off factor of 0.05. This because no considerable sharp variation was expected within the subsurface resistivities. A default damping factor of 0.15 was initially set, although the inversion allowed to increase the damping factor values at the lateral boundaries of the model to reduce edge effects (Tavakoli et al., 2016a). Since the sedimentary layers were expected to be oriented horizontally in the subsurface, with minor vertical sequences e.g. for the cryopegs, the vertical to horizontal flatness ratio (V/H) was adjusted to 1.00 to avoid biased flattening. The initial models did not demonstrate any irregular variation in the DCIP values from the deeper parts, therefore a default depth weighting factor of 1.05 was considered to compensate for the resolution

loss at greater depths (Tavakoli et al., 2016b). In the modified inversion, a robust data constraint with similar cut-off factor of 0.05 and a robust model constraint was used. The V/H flatness factor was reduced to 0.4 to examine the effect from emphasizing the dominant horizontally oriented anomalies. The damping factor was increased to 0.22 to account for the presence of noise in the data. The target limit for the RMS error was set to 7% during the inversion. For the inversion of the IP data, the program was set to calculate the IP damping factor from the Jacobian Matrix values. Integral chargeability inversion was used and similar model constraint as for the DC resistivity data were selected, i.e. smooth model constraints. The final inversion results and interpretations were presented with the smooth model constraint and using the default inversion setting parameters.

The inverted resistivity data indicate anomalies down to approximately 20 m below the ground surface. An intermediate resistivity layer can be identified within the top 3–5 m of the profile sections, followed by an underlying high resistivity layer with a variable thickness between 5 and 10 m. The high resistivity layer overlies an intermediate-high resistivity zone with ca. 1500 Ω.m resistivity, which is followed by a very low resistivity layer (ca. 10–50 Ω.m) at greater depth and down to a maximum depth of 26 m (Fig. 4a-I to 4f-I). The IP data were associated with high amounts of noise in most of the profiles, with weak or no IP anomalies indicated in the inversion results. These are most probably attributed to inversion artefacts and do not represent subsurface structures. The same applies to the resistivity data at shallow depths. Generally, the presence of inversion artefacts increases with increasing depths. However, in zones where resistivity or chargeability contrasts are high, the inversion may also produce artefacts near the anomalous body (Doyoro et al., 2021). Even though we applied the robust inversion algorithm (L1 norm), some artefacts are present in the near-surface parts of several resistivity profiles (see e.g. Fig. 4b-I). Insignificant IP anomalies can be observed with values ranging between 6 and 35 ms, these are related to the presence of disseminated and probably unfrozen chargeable materials such as clay (see e.g. Fig. 4b-II and 4b-II). The inversion result from profile SVAER05 indicates no IP signature (Fig. 4c-II).

5.2.2. DCIP inversion in AarhusINV– Gradient array profiles

To evaluate the differences between the inversion results of the different programs, all DCIP data were also inverted using the AarhusINV Ver.6.4.0.0.

AarhusINV offers the following four types of model regularization schemes for the inversion: layered, smooth (L2), blocky (L1), and sharp. We evaluated the inversion results using both L1 and L2 norms for the selected profiles. However, the final results of our study are only presented for the smooth inversion (L2) to allow comparison with the inversion results from Res2DINV. Inversion using the smooth L2 model has the advantage of flexibility in handling a varying number of stratigraphies and non-layered complex subsurface structures, e.g. inclined layer sequences, as these structures can be better detected using the L2 model norm as compared to three other types of model regularizations. We selected automatic IP processing which provides the possibility to filter out noisy or faulty IP decays based on the slope change and removes considerable parts of the decays. For the processing of all IP data, a full-wave filter was selected, and the maximum slope change was set to 0.2. Similar files as for the inversion of the Res2DINV were used in AarhusINV, i.e. the data after removal of the outliers. For the DCIP data, the 2D integral chargeability inversion with 20 layers and vertical model discretization ranging between 0.5 and 44.6 m was used. The inversion algorithm in AarhusINV runs by using the laterally constrained inversion (LCI). The L2 regularization smoothens the vertical changes in resistivity, resulting in a vertically smooth resistivity model. Starting values for resistivity, layer thickness, constraints, and chargeability were set to be selected automatically by the program in the auto-mode.

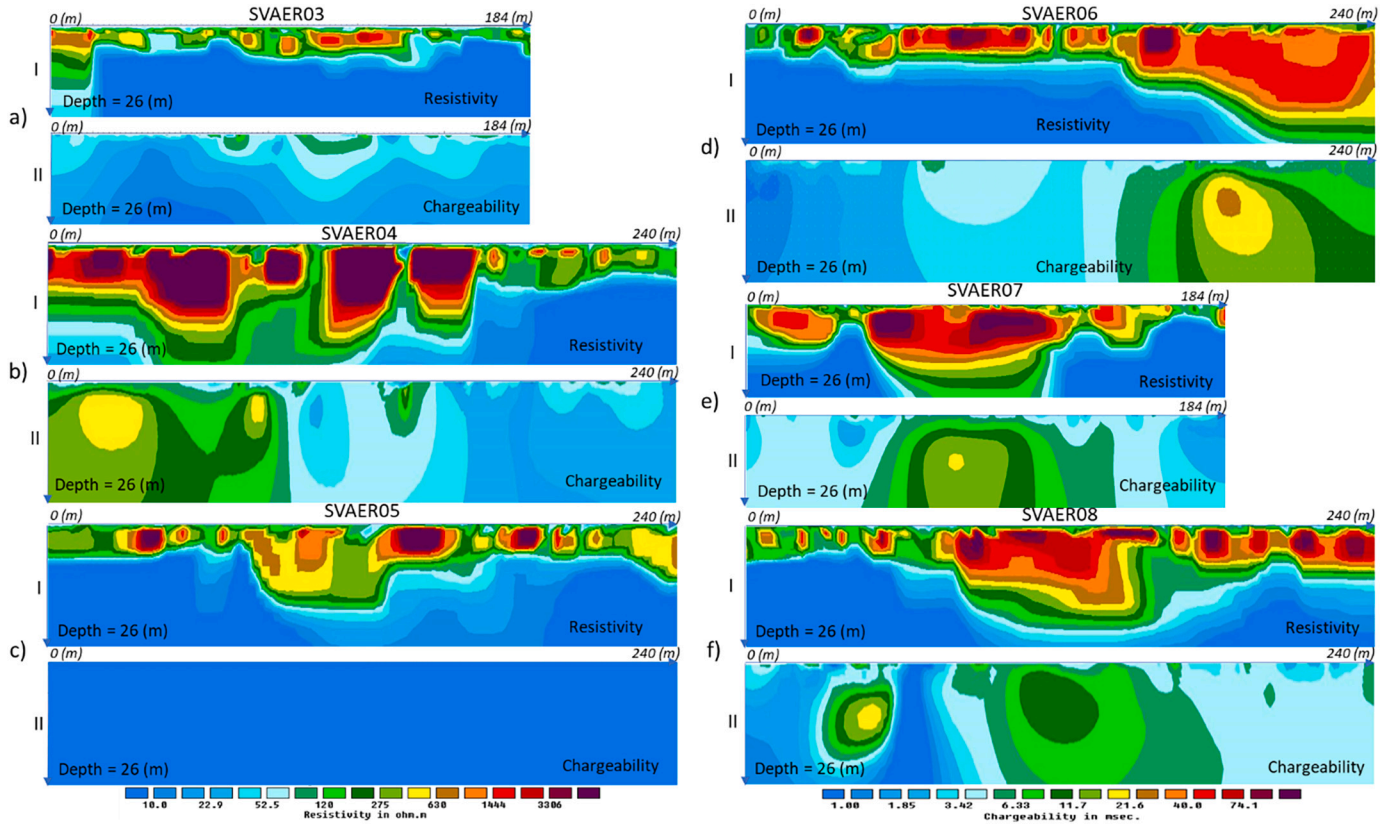

Fig. 4. Results from inversion of the Gradient array DCIP data in Res2DINV for profiles SVAER03-SVAER08. I represent the resistivity data and II the chargeability data. Distances along the horizontal axis (x) and vertical axis (depth) are given in meters (m).

Due to the often-low S/N ratio for the IP data, a uniform 5% standard deviation was applied during data import. Inversion was set to modify this value if high residuals were achieved after the initial inversion. The inversion results for the DCIP data in AarhusINV were calculated and presented in the form of residual values.

The results from the inversion with AarhusINV indicate similar characteristics as those inverted with Res2DINV. The main difference is the vertical exaggeration of the intermediate and high resistivity anomalies in the AarhusINV results (Fig. 4a-I to 4f-I and Fig. 5a-I to 5f-I). Profile SVAER06 demonstrates considerable variations in the resistivity models resulting from the two inversion programs, demonstrated by a larger coverage of the high resistivity anomaly in the centre of the profile as compared to the inversion results from Res2DINV (Figs. 4d-I and 5d-I). The IP anomalies from the inversion of the IP data indicate values which are within the range for common IP values for sediments, i.e. 10–100 msec. High chargeability anomalies in this study are often observed where high resistivity values are present. The IP results for profile SVAER05 which was blank in Fig. 4c-II, here indicates several weak anomalies close to the surface (Fig. 5c-II).

5.2.3. *Inversion algorithms and the outcome parameters*

The inversion output parameters from AarhusINV and Res2DINV cannot be compared directly. While the RMS error in Res2DINV indicates the distribution of the percentage difference between the logarithms of the observed and calculated apparent resistivity and chargeability values, the total residual value in AarhusINV is calculated proportionally to the uncertainty, i.e. as the standard deviation.

In Res2DINV, the root-mean squared (RMS) error is calculated based on an optimization function which tries to minimize the difference between measured and calculated apparent resistivity/IP data by adjusting the resistivity/chargeability of the model blocks. However, a model with the lowest possible RMS error does not necessarily depict the best model from a geological perspective, this can be particularly observed in the RMS values from the inversion of the IP data. The maximum number of iterations was set to five by default. However, since the model was not converged at the 5th iteration, the inversion algorithm was allowed to continue until the RMS convergence limit of 5% was reached. The inversion output parameters, including the number of iterations, RMS error, block sensitivity for the DCIP profiles are listed in Table 4.

The block sensitivity data indicates average sensitivity of the model blocks, i.e. a measure of the information about the resistivity of the blocks, used in the inversion. The higher the sensitivity value, the more reliable is the DCIP model. In general, blocks near the surface indicate higher sensitivity values because of the larger sensitivity function closer to the electrodes. In general, Gradient array data provide higher sensitivities compared to the Wenner array data (see e.g. SVAER05 vs SVAER05-W; Table 4). In the Gradient array, concentration of the high sensitivity values is greater near the current electrodes, whereas for the

Table 4
Inversion parameters from Gradient and Wenner array DCIP data in Res2DINV.

Profiles	Number of iterations	resistivity RMS error %	IP RMS error %	Average model block sensitivity - Res	Average model block sensitivity - IP
SVAER03	6	2	0.5	2.36	4.6
SVAER04	6	4	0.5	2.1	1.8
SVAER05	6	1.7	0.1	2.3	2
SVAER05-w	6	1.6	0.5	0.6	0.6
SVAER06	6	2.4	0.4	1.5	1.7
SVAER06-w	6	3.3	0.5	0.5	0.5
SVAER07	6	1.6	0.4	2.2	4
SVAER08	6	2.3	1	2.2	1.9

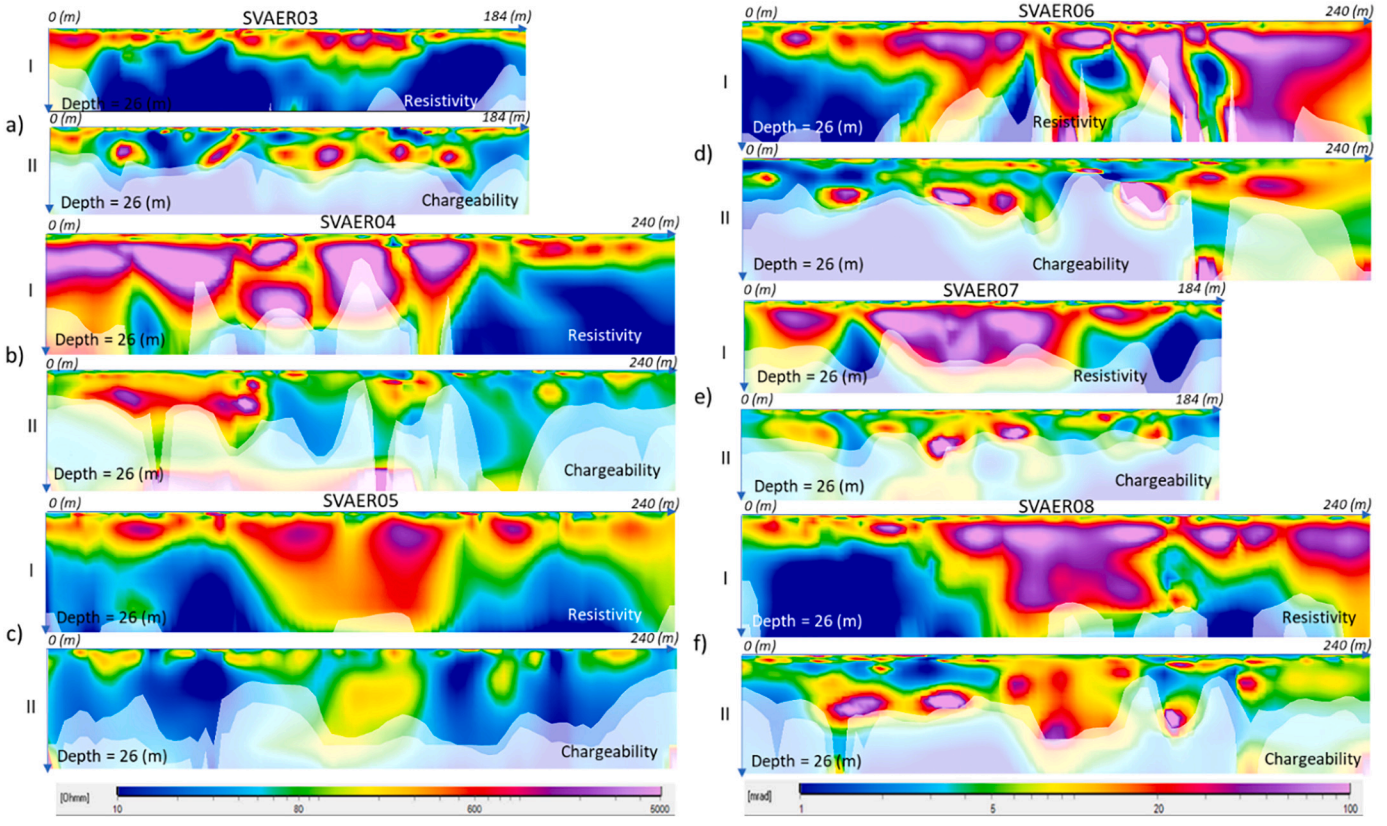

Fig. 5. Results from inversion of the Gradient array DCIP data from AarhusINV for profiles SVAER03–SVAER08. Distances along the horizontal axis (x) and vertical axis (depth) are given in meters (m).

Wenner array the highest sensitivity values are observed between the potential electrodes. Gradient array data provide a more homogenous sensitivity distribution closer to the surface. Model sensitivities from deeper parts of the subsurface indicate higher sensitivity for the Wenner array data as compared to the sensitivity values from similar depths in the Gradient array data.

The optimization process in the inversion algorithm for AarhusINV attempts to minimize the model norm and data misfit which is indicated by the total residual value (Table 5). A residual value of 1 indicates that the data are being fitted exactly within the standard deviation (the difference between measured data and forward calculations for the last iteration is equal to the standard deviation). Therefore, a residual value of $\leq$1 signifies that the inversion is fitting better compared to when the residual value is 1 and vice versa that the fit is weaker for values $\geq$1. The values for the total residual of the DCIP data in AarhusINV are relatively low and range between 1.6 and 5.5. The number of iterations required for the optimization process in AarhusINV was higher compared to Res2DINV (Table 5).

6. Discussion

6.1. Comparison between the results from Res2DINV and AarhusINV

Inversion results of DCIP data in Res2DINV and AarhusINV have been compared in several studies for identical datasets: Hellman et al. (2016) compared the inversion response from two case studies in Res2DINV and AarhusINV in an environment dominated by sediments. The first model was for a river channel where coarse grain sediments e.g. sands and gravels, were surrounded by silty and clayey sediments, and the second model included a dipping layer model. The inversion results from the two inversion algorithms despite discretization differences, demonstrated similar outputs for the buried channel model, designating nearly identical geological interpretations for the identical features. Minor underestimation of the depth of the river channel was observed in the model results from both inversion programs. For the dipping layer, Res2Dinv tends to extend the blocks vertically with barely a clear indication of dipping, whereas results from AarhusINV were closer to the actual geometry of the dipping layer. In another study (Aarhus Software Report, 2018), the inversion results from Res2DINV with the robust norm (L1) were compared to the results from AarhusINV using the sharp and smooth (L2) norm. The inverted model using the L2 norm demonstrated a more realistic geological model in AarhusINV with lower misfit compared to the robust model. Although the inverted section using the robust inversion in Res2DINV provided a good model fit associated with a low RMS error, the study summarized that the inversion outcomes are not quantitatively comparable for AarhusINV and Res2DINV due to the different algorithms used, and subsequent differences in the inversion log information. Fiandaca et al. (2012) concluded that the result from AarhusINV's laterally constrained inversion was to be preferred to result from RES2DINV. The argumentation being that the latter does not allow the implementation of the transmitter waveform. This generates a significant bias in the parameter retrieval in terms of parameter ranges and anomaly patterns, which could be observed as well in the result of the here presented study.

In this study, DCIP inversion results for the profiles SVAER05 and SVAER06 were compared for Gradient array data in AarhusINV and Res2DINV (Fig. 6). In profile SVAER05, resistivity anomalies are sharper, with a distinctive pattern in the results from Res2DINV compared to the AarhusINV results, which can be related to the applied smoothness functions (Fig. 6a-I and 6b-I). The IP data indicate small and insignificant anomalies in the results from both profiles, yet are more pronounced in AarhusINV than in Res2DINV (see e.g. Fig. 6c-II and 6d-II). The high IP anomalies are expected to reflect clay content in the sediments within the upper parts of the stratigraphy. These anomalies often coincide with high resistivity values (Fig. 6a-I, 6a-II, 6c-I and 6c-II) which their appearances within the top five meters of the subsurface is possibly related to the presence of the silts and clays within the active layer, or the cryopeg where the frozen-unfrozen interface allows minor mobility of ions, which results in an elevated IP response compared to the upper parts. Inversion results for the DC resistivity data for profile SVAER05 in AarhusINV suggest a relatively greater depth extent for the high resistivity zone at ca. x = 100 m compared to the corresponding anomaly indicated in Res2DINV (Fig. 6a-I and 6b-I). However, although the Res2DINV seems to be less capable to resolve anomalies from deeper parts of the models, another possible reason for little information in the results of the Res2DINV could be related to the presentation of the data, since the colour scale is not detailed enough to indicate the small anomalies within the deeper parts of the sections. Similar to profile SVAER05, the IP anomalies in profile SVAER06 are more distinctive in the results from AarhusINV (Fig. 6c-II and 6d-II). Presence of likely inversion artefacts (visible as small resistivity areas at shallow depths) can be observed in the results from Res2DINV (Fig. 6b-I), at very shallow and very deep areas of the IP sections (Fig. 6c-II).

6.2. Comparison between the results from Gradient array data vs Wenner array data – AarhusINV

Since AarhusINV was selected for the presentation of the final results and interpretations, comparison between the inversion results from Gradient and Wenner array data for the profiles SVAER05 and SVAER06 is only done in AarhusINV. In general, the results indicate similarities for the resistivity data, whereas the IP data can be separated by major distinctions. Data acquired from the Wenner array are more sensitive to vertical variations in the subsurface resistivity below the centre of the array, but less sensitive to horizontal resistivity variations. Considering the horizontally layered characteristic of the subsurface in the area, using the Wenner array was a suitable choice for this study. The geometric factor of an array is indirectly related to its signal strength. Since the Wenner array has the smallest geometric factor among all arrays, it is expected to provide the highest signal strength. The electromagnetic (EM) coupling is likely to occur between the two dipole pairs, especially if they are separated by a large electrode spacing, or around the connecting cables and at higher voltage frequencies. Other sources of the EM coupling can be heterogeneity of the subsurface and effects from man-made objects in or near the survey area. Since the artificial EM coupling was avoided during the survey, the noise in the data is most likely produced from subsurface material. An alternative interpretation is that they represent inversion artefacts. In IP surveys, the EM coupling between the IP transmitter and the receiver circuits becomes more important to account for, particularly for surveys with great investigation depths (Tavakoli et al., 2016b). Considering the shallow investigation depth in this study, this phenomena is unlikely to be a source of the observed noise. Minor discrepancies can be observed in the resistivity data from the two programs, where the high resistivity anomaly in the Wenner profile at the centre of the profile SVAER05 indicates a dipping trend and a larger volume for the anomaly related to high resistivity sediments at x = 100 m and 160 m, compared to its identical

Table 5
Inversion parameters resulted from inversion of the DCIP data in AarhusINV.

Profiles	Number of iterations	Total resistivity residual	Total IP residual	Total number of model parameters
SVAER03	10	1.8	5.3	3240
SVAER04	11	2.3	2.9	3240
SVAER05	7	3.5	4.6	3240
SVAER05-w	10	3.1	3.3	3240
SVAER06	15	4.6	4.7	3240
SVAER06-w	8	5.5	4.4	3240
SVAER07	9	1.6	2.7	3240
SVAER08	14	4.1	1.7	3240

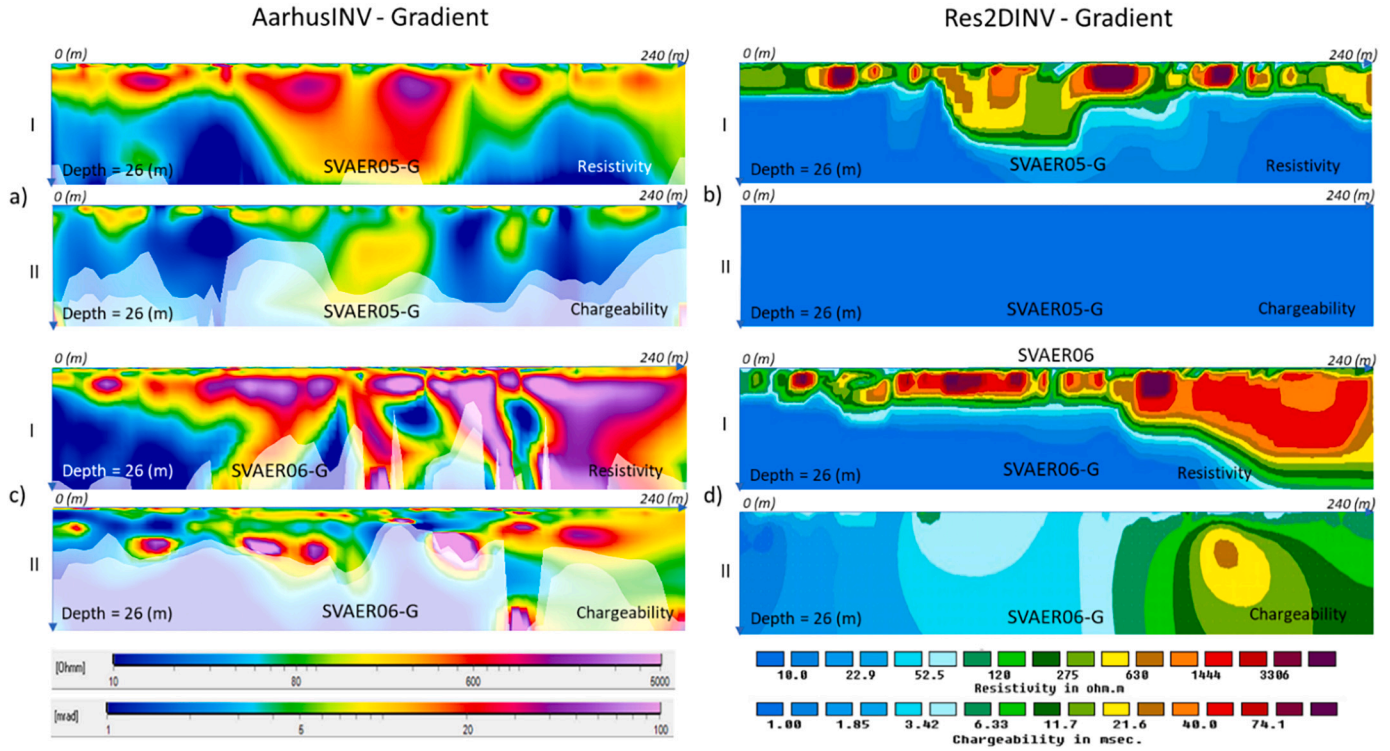

Fig. 6. Comparison between the inversion results from Gradient array (G) data in AarhusINV and Res2DINV. a) Inversion results for profile SVAER05-G in AarhusINV. b) Inversion results for profile SVAER05-G from Res2DINV. c) Inversion results for profile SVAER06-G in AarhusINV. d) Inversion results for profile SVAER06-G in Res2DINV. I and II indicate resistivity and chargeability data, respectively. Distances along the horizontal axis (x) and vertical axis (depth) are given in meters (m).

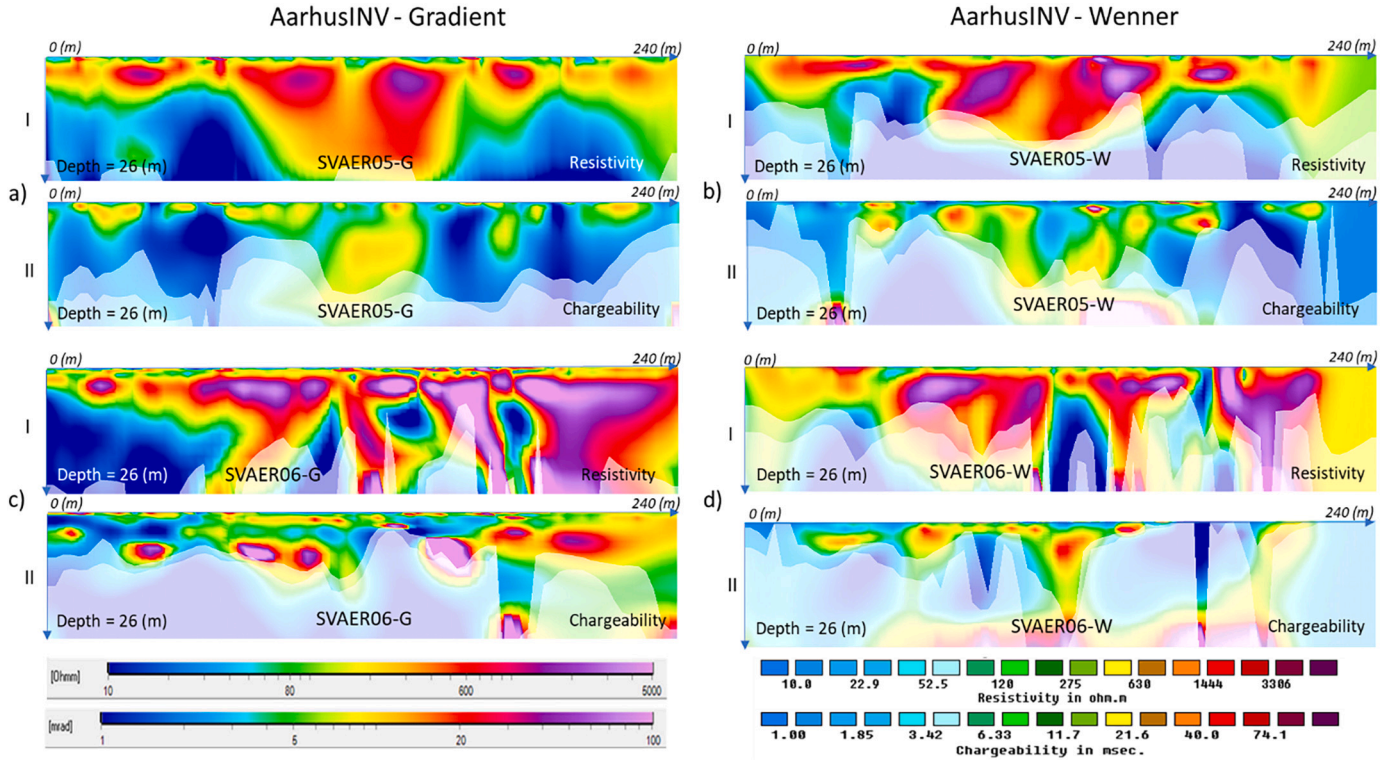

Fig. 7. Comparison between Gradient (G) and Wenner array (W) results in AarhusINV. a) Inversion result from Gradient array for profile SVAER05-G, b) Inversion results from Wenner array for profile SVAER05-W. c) Inversion result from Gradient array for profile SVAER06-G. d) Inversion result from Wenner array for profile SVAER06-W. I and II indicate resistivity and chargeability data, respectively. Distances along the horizontal axis (x) and vertical axis (depth) are given in meters (m).

anomaly in the Gradient array profile (Fig. 7a-I and 7b-I). This can indicate that the high resistivity layer, interpreted as frozen soil, is extending down to ca. 10 m depth, which is deeper compared to what was indicated in the results from the Gradient the array data.

IP data from the Wenner array demonstrate further details in the results for profile SVAER05 compared to the Gradient array data. The IP anomaly for profile SVAER05-W indicates a large number of high IP anomalies closer to the surface which can also be observed in the result from the Gradient data, although as weaker and less distinctive anomalies than expected. This is due to the stronger signal acquired in the Wenner array data, in an environment where little induced polarization effect is present (Fig. 7a-II and 7b-II). In profile SVAER06-W, the high resistivity anomaly at approximately x = 180 m does not start immediately below the surface (Fig. 7d-I). Also, the conductive zones at ca. x = 0–60 m and x = 110 m indicate larger anomaly extents compared to the Gradient array data (Fig. 7c- I and 7d-I). Due to the asymmetric nature of the Gradient array survey, the asymmetry observed in the anomalies are probably closer to the actual subsurface stratigraphy in the Wenner data (Fig. 7b-I and 7d-I). Gradient array IP data for profile SVAER06 indicate that the two high chargeability layers sandwich a low chargeability zone, within the top 10 m of the subsurface. This trend cannot be seen in the Wenner array results, however. This discrepancy in the results might be related to sub-vertical or vertical trends of the anomalous structures, which may have been weakly indicated in the results in Wenner array data (Fig. 7c-II and 7d-II).

In DCIP surveys using the Gradient array, the higher sensitivity is expected to concentrate near the current electrodes and less at the centre of the profiles. This is almost opposite to the higher sensitivity in Wenner arrays, which often is observed beneath the potential electrodes and reduced near the current electrodes. This makes simultaneous application of the two surveys good complements to each other and can explain one of the reasons for the observed discrepancies in the DCIP anomalies, especially within the upper parts of the data measured in Gradient and Wenner arrays (Fig. 7a, b,c, and d).

6.3. *Petrophysical parameters of the sediments and it's link to the DC resistivity data*

Sediment's petrophysical data from earlier in-situ laboratory experiments indicate a correlation with the electrical properties, which helps to constrain observations in the field data (Tavakoli et al., 2012). Areas of the subsurface sedimentary stratigraphy which are associated with high values of porosity, water saturation, water salinity and finer grain size, are expected to indicate lower resistivity responses. Lower freezing point temperature is also expected to be associated with low resistivities, which is in correlation with water salinity, since higher water salinity leads to lower freezing points. Therefore, we only study the effect from water salinity in the resistivity of the sediments, out of these two parameters. Two of the wells (A4 and A5; Fig. 1) nearly intersect with profile SVAER04 and indicate correlation between the sediment's petrophysical parameters and the resistivity data. At depths between 9 and 14 m in well A4, and 11–17 m in well A5, respectively, the highest simultaneous value for the porosity, water saturation and water salinity and intermediate-low grain size (Fig. 8a-I, 8a-II; A4 and, Fig. 8b-I and 8b-II; A5) coincide with the transition from high resistivity values in the top layer to low resistivity values immediately below Fig. 8a-III and Fig. 8b-III). This correlation confirms that the micro-scale physical parameters obtained from in-situ experiments and resistivity data from field geophysical surveys in macro-scale can be jointly applied to validate interpretation. The correlation between the sediment's physical properties and measured resistivities also indicates that one dataset can be individually used to infer information about the other dataset, where direct measurements are not possible.

1.1 3D data integration in Leapfrog and general model of the subsurface at the study site

Integration of the DCIP data in Leapfrog's 3D environment indicates a relatively consistent pattern for each set of the three sub-parallel profiles, i.e. for the NE-SW trending profiles SVAER03, SVAER07, and

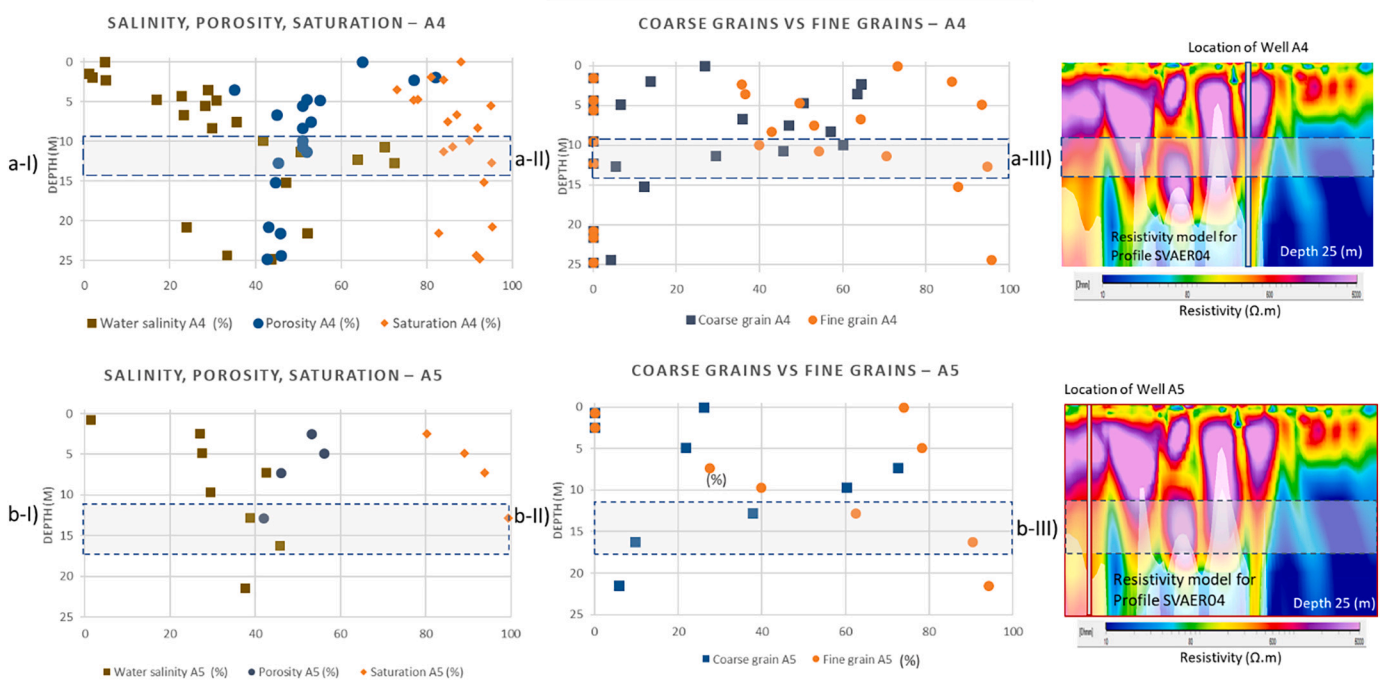

Fig. 8. The depth at which sediment's water salinity, saturation and porosity indicate high and grain size indicates intermediate-low in wells A4 and A5 which associate with low resistivity values in the intersecting profile SVAER04. a-I) water salinity, sample porosity and water saturation for the well A4, a-II) coarse grain size vs fine grain size for well A4, a-III) DC resistivity model for profile SVAER04, b-I) water salinity, sample porosity and water saturation for well A5, b-II) coarse grain size vs fine grain size for well A5, b-III) DC resistivity model for profile SVAER04 (source of data for plots a-I, b-I, a-II and b-II from Gilbert et al., 2019).

SVAER04, and the NW-SE trending profiles SVAER05, SVAER08, and SVAER06, respectively (Figs. 1, 9a and b). The resistivity value of the sediments in the area range between 10 and 5000 Ω·m. The general pattern of the resistivity data from each group of the three sub-parallel profiles SVAER03, SVAER07, and SVAER04 and profiles SVAER05, SVAER08, and SVAER06 indicates an approximately consistent resistivity signature. However, the latter group yield a slightly lower thickness for the high resistivity layer to the NW compared with their SE end (Fig. 9a). An interesting characteristic of the high resistivity layer across the study area is the undulating pattern: the thicker high resistivity anomalies are often interrupted by minor vertical extension of the underlying conductive layer towards the surface, which is related to the variation in sediment composition and/or their physical properties near the cryopeg interface (Fig. 9a).

The IP response is in general weak and the outlined IP anomalies are probably associated with noise. The IP value of the sediments in the area ranges between 1 and 100 ms. IP anomalies appear as a thin layer with low to intermediate values closer to the surface which depict the active layer followed by intermediate-high chargeabilities down to 10 m depth with higher salt concentration compared to its overlying layer (Fig. 9b). Occasional occurrences of the low chargeability zones within the top 10 m of the subsurface which can be observed in profiles 3, 6 and 8 which is related to the frozen soil and limited mobility of the ions which reduces the IP response (Fig. 5a-II, 5d-II and 5f-II). The deepest IP response can be observed in profile SVAER08 where the high IP anomaly continues at depth down to ca. 20 m which is coincident with the high resistivities and indicates greater thickness for the low-salt content formation in that part (Fig. 5f-II).

Based on the results from the inversion of the DCIP data, the following zones were identified within the sedimentary stratigraphy of the study site in Adventdalen (Fig. 9c and d):

i. A thin top layer identified as active layer-silt which together with its underlying sands indicates an intermediate resistivity (200–300 Ω·m), reflecting the unfrozen formation at the time of measurements. This part of the section indicates low-intermediate IP values. The thickness of the entire layer does not exceed 5 m at depth below the surface, but often ≤3 m.
ii. A high resistivity layer (2500–5000 Ω·m) which depicts the frozen soil with variable thickness of 3–10 m and is often associated with high IP anomalies which are either related to the presence of clayey sediments, high salt content or a combination of the two. An intermediate resistivity anomaly (240–1200 Ω·m) separates the high resistivity layer on top from the low resistivity below and indicates large thickness (ca. 13 m) within the central part for most of the profiles compared with lower thickness (ca. 5 m) to the sides of the profiles (Fig. 9a).
iii. Cryopeg with low resistivity and low chargeability values of 40 Ω·m and 3 ms respectively, can be observed at depths ca. 13 m with larger volumes in the sides of the profiles. The low chargeability of these cryopegs is probably related to the small surface area of their sedimentary host formation which results in low polarization effects.
iv. A low resistivity zone (10–20 Ω·m) which is composed of clay-unfrozen soil sediments at depth below 13 m is associated with low chargeability (1–5 ms), which can be related to either the frozen ground which limits the ion mobilities or low S/N ratio for the IP data.

6.4. Depth slice models

Based on the results from interpretation of the Gradient array DCIP data, a 3D model of the subsurface was created down to 26 m in Leapfrog. Description of the sedimentary stratigraphy from wells A3 to A5

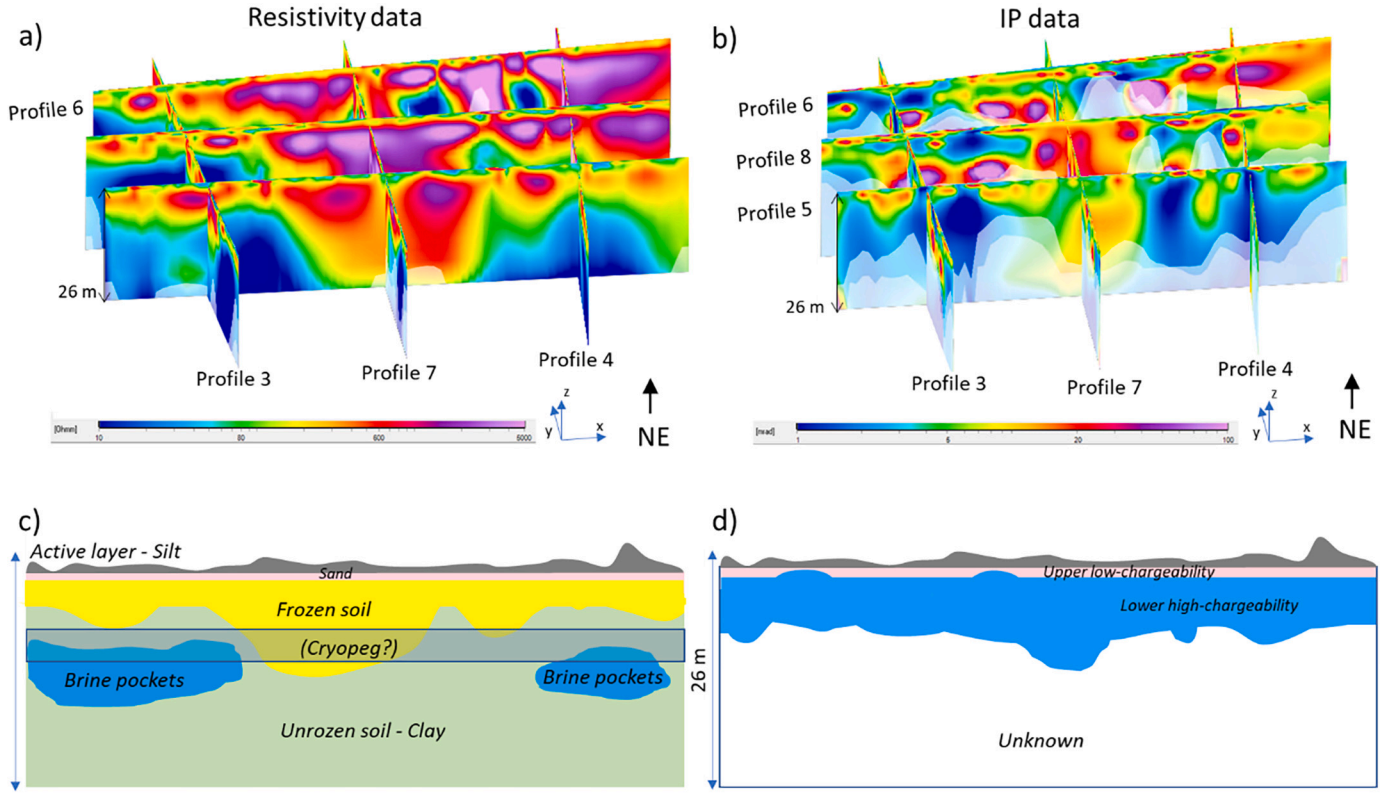

Fig. 9. Integration of the DCIP data in Leapfrog's 3D visualization and the inferred general subsurface model. a) Integration of the resistivity data for 3D interpretations in Leapfrog. b) Integration of the IP data for 3D interpretations in Leapfrog. c) the modelled section inferred from resistivity interpretations. d) the modelled section inferred from IP interpretations.

were also incorporated in the modelling for calibration of the DCIP data where relevant. However, due to the sparse distribution of the wells in the area, the well data provided minor input to the 3D models and therefore properties of the 3D models were mainly understood based on interpolations from the DCIP data. The 3D model helps to infer the subsurface information from e.g. parts of the study area where no DCIP profile coverage was available (Tavakoli et al., 2021).

The 3D resistivity model is sliced at different depth levels from the surface down to 26 m and indicates the following sedimentary stratigraphy (Fig. 10): (i) active layer and top sand, (ii) frozen soil with low salt content, (iii) cryopeg zones, (iv) clayey-unfrozen soil sediments. The result from the sliced models show that the active layer and sand do not extend to a depth greater than 5 m. Clayey frozen soil with low salt content are thick, extending from ca. 5 m depth to 10 m. Cryopegs can be observed down to 20 m depth (Fig. 10b–10e). However, due to the large distance between the blue zones representing the cryopeg (based on the interpretation of the DC resistivity data), and due to the large distance between the wells, the generated cryopeg zones are indicated with a larger extent than their real presence, which is partly an artefact (see e.g. Fig. 10b and c). The cryopeg zone is expected to be present at depths greater than 10 m, within the interface between the frozen soil with low salt content and the clayey-unfrozen soil sediments. The model is less reliable in the areas far from the wells, and also within the deeper parts of the models, i.e. $\geq$ 20 m (Fig. 10e and f).

The 3D model inferred from IP interpretations was generated based on a simple three-layered model consisting of (i) an upper low-chargeability, (ii) a lower high-chargeability and (iii) no data or unknown layers. Due to an overall insignificant IP signature from most of the studied sediments in this study, and also a weak S/N ratio from deeper parts of the IP data, the generated IP model provided less information compared with the resistivity model and, therefore, correlating the IP anomalies to different types of sediments is not straight forward. Nevertheless, the transition from low-chargeability on top to the high-chargeability anomalies below, is distinctive between 0 and 10 m depth (Fig. 11a–11c). Below 15 m depth, no IP anomaly is observed in the sliced models, which is seen to be due to the reasons explained earlier (Fig. 11d–11f).

Among the sediments presented in the study area, clay is expected to generate the strongest IP signal, whereas the coarser grain sediments such as sand and gravel produce a weak IP signal. However, since the IP effect is controlled by multiple parameters, making a simple conclusion about the sediment types would be inaccurate. This is for instance the case for the frozen clays which often indicate less water saturations and less ion mobility, whilst it does not always provide a lower IP effect compared to the unfrozen sands with greater water saturation and higher ion mobility. The frozen soil with great amount of sands and low

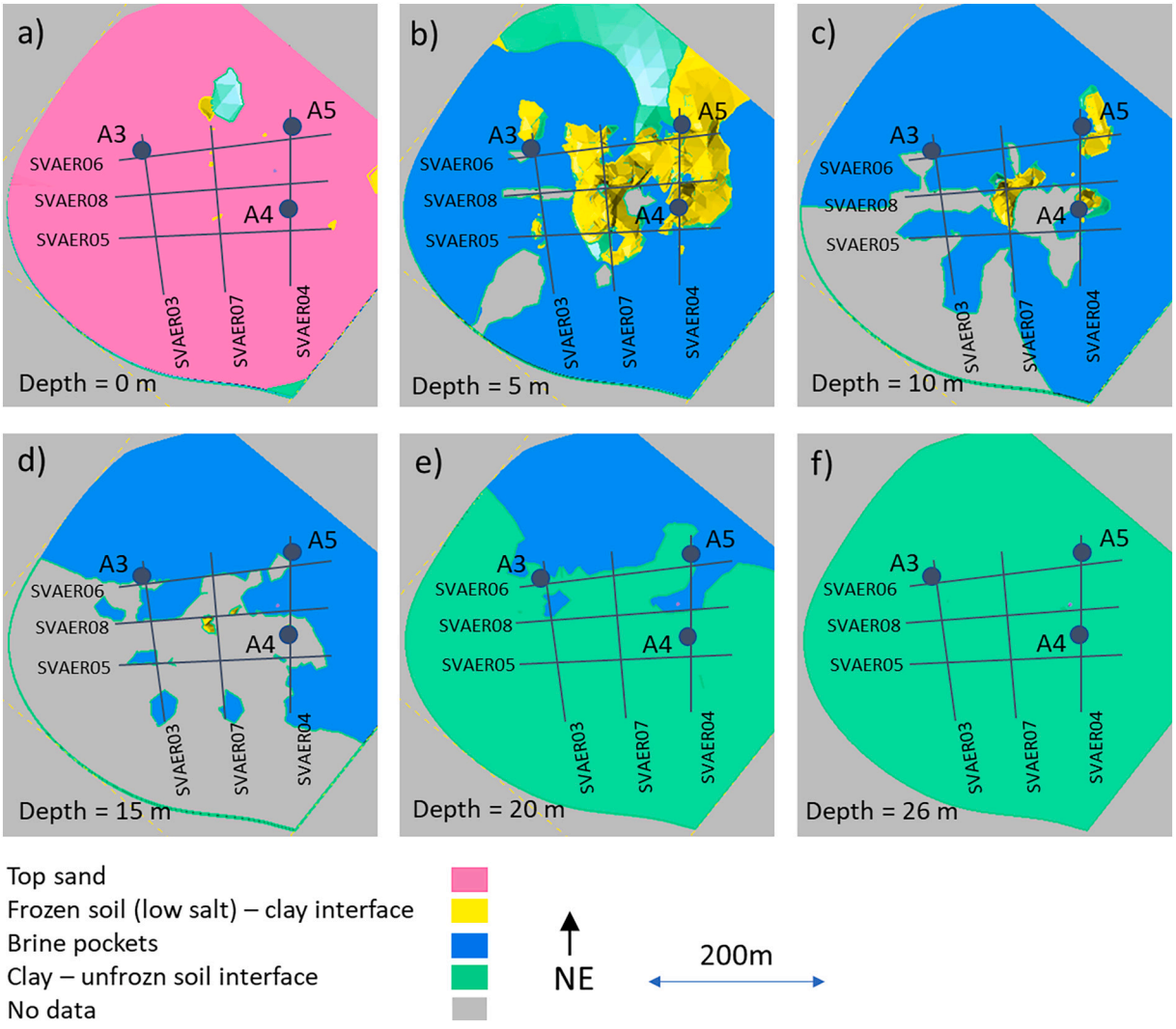

Fig. 10. The sliced depth layers created from 3D subsurface model inferred from interpretation of the DC resistivity data; a) At the surface, b) at 5 m depth, c) at 10 m depth, d) at 15 m depth, a) at 20 m depth and f) at 26 m depth. The depth slices indicate variations in the resistivity response of the stratigraphy down to 26 m depth. Location of the wells A3 to A5 is indicated on the sliced depth layers.

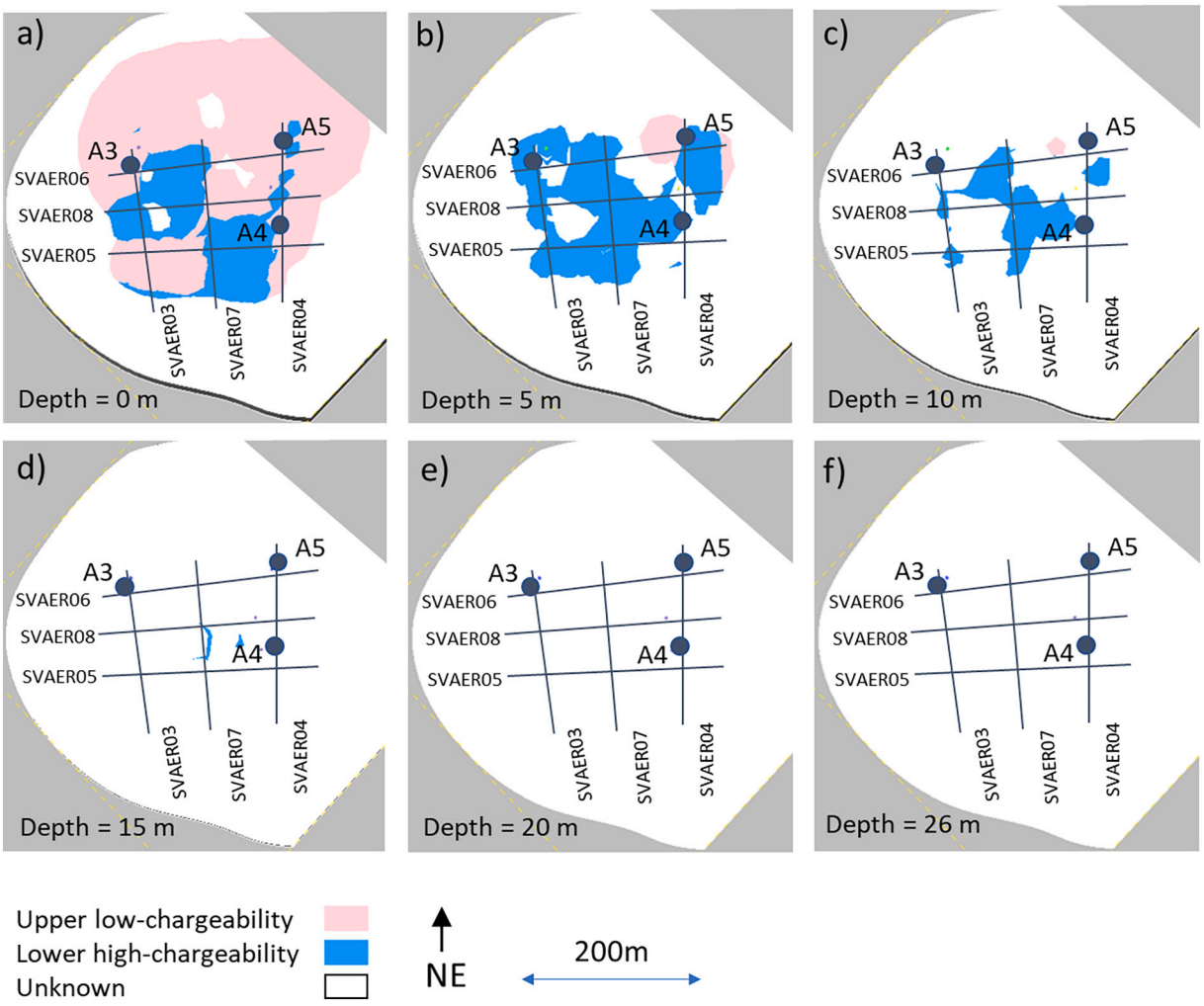

Fig. 11. The sliced depth layers created from 3D subsurface model inferred from interpretation of the IP data; a) at the surface, b) at 5 m depth, c) at 10 m depth, d) at 15 m depth, a) at 20 m depth and f) at 26 m depth. The depth slices indicate variations in the IP response of the stratigraphy down to 26 m depth. Location of the wells A3 to A5 is indicated on the sliced depth layers.

salt content at deeper parts of the model (Fig. 11c) indicate lower IP signature compared with the upper parts of profiles, where clays closer to the surface are associated with high chargeability values (Fig. 11a).

6.5. Comparison between the inverted DC resistivity data and cross-sections generated from 3D subsurface modelling

The reproducibility of the generated 3D resistivity models was verified against the inverted resistivity sections; that is, cross-sections generated from 3D solid stratigraphical models were compared with the inverted DC resistivity sections for all profiles and down to 26 m depth (Fig. 12). The result indicates a good correlation between the distinct stratigraphic layers inferred from the inversion of the DC resistivity data and the generated cross-sections, i.e. the thickness variation for the active layer and top sand, frozen soil, cryopegs and the clay-unfrozen soil sediments are consistent (Fig. 12a–12f). The cryopegs indicated in blue in some profiles appear as continuous layers (Fig. 12c-II and 12d-II). A relatively large spacing between the profiles sometimes resulted in discrepancies in between the cross-sections and actual resistivity data from the field. Nevertheless, using this approach, one can generate and access the cross-sections inferred from 3D subsurface model from even outside the resistivity profiles.

7. Conclusions

Comparison between the two inversion programs Res2DINV and AarhusINV, yielding overall similar anomaly patterns for most of the profiles, concluded that AarhusINV generated a smoother and more consistent anomaly pattern for the DC resistivity data. Thus, resolving the architecture of the sedimentary layers in a more geologically meaningful way as compared to the Res2DINV results. The IP response of the profiles was in general weak due to: (i) low IP effect of the survey environment, (ii) partially frozen subsurface, (iii) nearly homogenous subsurface, and (iv) signal loss at deeper parts of the ground owing to the small electrode spacing used during the field survey. The IP data were demonstrated with higher precision in AarhusINV as compared to Res2DINV, as the latter failed to produce noticeable IP anomalies. Results from the Wenner array favours that of the Gradient array, as it provides higher signal strength which aides to resolve the features of interest at deeper parts of the model.

Four distinct layers were identified based on the inversion results from the DCIP data although with greater contribution from DC resistivity data, consisting of (i) a thin active layer consisting of silt and sand with intermediate resistivity, (ii) a high resistivity layer which depicts the frozen soil with 3–10 m thickness and the intermediate-high resistivity anomaly at the interface between frozen and unfrozen soil sediments which probably depicts the cryopeg, (iii) cryopegs with high

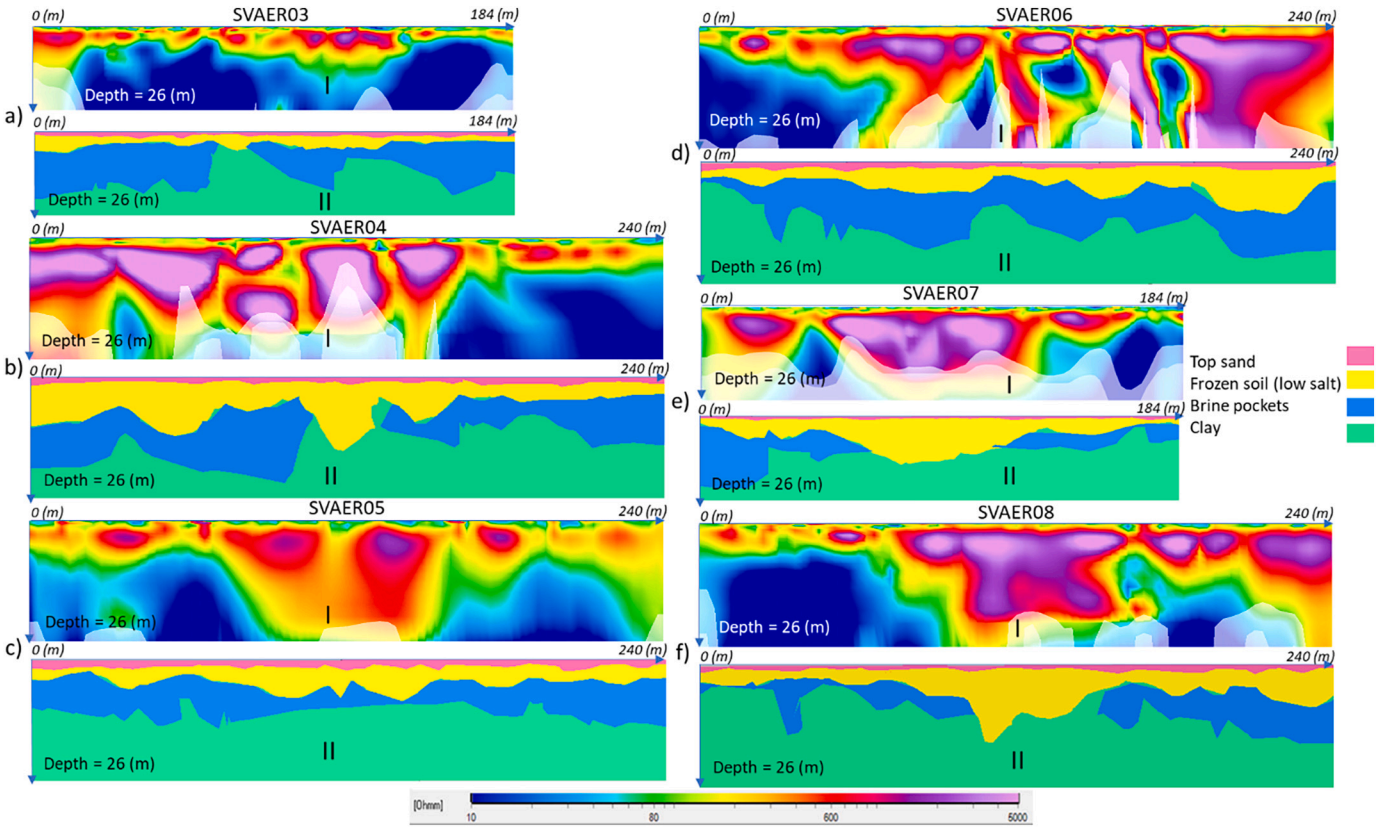

Fig. 12. Comparison between the inverted resistivity profiles and corresponding cross-sections generated from 3D subsurface modelling in Leapfrog. Distances along the horizontal axis (x) and vertical axis (depth) are given in meters (m).

salt content indicated by low resistivity and low chargeability, and (iv) unfrozen clayey soil sediments with low resistivity located at depth between 13 and 26 m. The IP data could differentiate the low IP response of the active layer, consisting of sand on top and in parts the unfrozen soil sediments which is interpreted as cryopeg zone.

Studying the physical parameters from three wells including porosity, water salinity, water saturations and sample's grain size, demonstrated correlation with the electrical properties of the sediments, particularly with the DC resistivity data. Coarse-grained sediments with lower salt content, low porosity and hence lower degree of water saturation often associate with higher resistivities, which was observed in well A4 and profile SVAER04. This link can be used as a promising tool to indirectly characterise the subsurface using only one of the alternative methods, and at a lower cost where no additional data is accessible. Conducting the IP survey in an area with low IP effect and/or close electrode spacing, resulted in weak and sometimes no IP signal from deeper parts of the profiles. Nevertheless, the IP data particularly from the Wenner array provided information about several anomalies: an upper low-chargeability anomaly corresponding to the active layer and sands, and a lower high-chargeability anomaly related to the lower parts of the unfrozen clays and upper boundary of the cryopeg.

The depth slice models and model reconstruction in Leapfrog helped to provide information from outside the DCIP profiles and could validate some of the earlier interpretations. The 3D model of the subsurface sedimentary stratigraphy was created based on the interpretations from DCIP data and further constrained with well physical parameters which helped to image the distribution of the sedimentary formations down to 26 m depth in Adventdalen.

The findings in this study can be used to better understand the environmental, geotechnical and engineering problems associated with the presence of cryopegs in Adventdalen, and potentially other cryopeg affected areas in the Arctic.

Data availability

All data which were used in this work including DCIP and petrophysical data are stored and available at the internal data repository of the NGI.

Authors statement

Many thanks for taking your time and reading through our manuscript and providing valuable technical comments. We truly appreciate your kind efforts which we believe helped to improve the quality of our work. Below, we try to address your comments and suggestions thoroughly. In addition to your comments, we have modified other parts of the main texts and Figures considerably to improve the quality of the paper. Our descriptions/comments to the reviewer's comments are provided below with bullet points and, where applicable, the modified text is provided in dark blue text in Italics in this document.

Declaration of Competing Interest

The authors declare that they have no known competing financial interests or personal relationships that could have appeared to influence the work reported in this paper.

Acknowledgements

This study was conducted at the Norwegian Geo-Test Site (NGTS) in Adventdalen on Svalbard. The NGTS project has been funded by the Research Council of Norway (Infrastructure grant no. 245650/F50). Field investigations in 2020 were supported by the Svalbard Science Forum (grant no. ES669737, RiS ID 11564). Data processing, modelling and compilation of the manuscript was supported by the Norwegian

Geotechnical Institute through its basic funding from the Norwegian Government (GBV 2020 and 2021). The authors wish to thank Sebastian Sikora (UNIS) for his logistical support in Longyearbyen. We would also like to thank Heidi Hefre, head of the geosurveys group at NGI for all of the supports during this project.

References

Aarhus Software Report, 2018. Sharp Model Inversion Setup for Inversion of Geophysical Data - Guidelines and Examples. HydroGeophysics Group Department of Geoscience, Aarhus University, Denmark.

Aarhus Workbench, 2021. Available online at. https://agscloud.dk/AGS/Product%20Brochures/AarhusWorkbench.pdf.

Arenson, L.U., Springman, S.M., Sego, D.C., 2007. The rheology of frozen soils. Appl. Rheol. 17 https://doi.org/10.1515/arh-2007-0003.

Auken, E., Christiansen, A.V., Kirkegaard, C., Fiandaca, G., Schamper, C., Behroozmand, A.A., Binley, A., Nielsen, E., Effersø, F., Christensen, N.B., Sørensen, K., Foged, N., Vignoli, G., 2015. An overview of a highly versatile forward and stable inverse algorithm for airborne, ground-based and borehole electromagnetic and electric data. Explor. Geophys. https://doi.org/10.1071/EG13097.

Christiansen, H.H., Gilbert, G.L., Demidov, N., Guglielmin, M., Isaksen, K., Osuch, M., Boike, J., 2019. Permafrost Temperatures and Active Layer Thickness in Svalbard during 2017/2018 (PermaSval) 2018, pp. 236–249.

Cyril, C.O., 2013. Sensitivity and resolution capacity of electrode configurations. Int. J. Geophys. 2013, 14–15.

Dahlin, T., Zhou, B., 2004. A numerical comparison of 2D resistivity imaging with 10 electrode arrays. Geophys. Prospect. 52, 379–398. https://doi.org/10.1111/j.1365-2478.2004.00423.x.

de Grandpré, I., Fortier, D., Stephani, E., 2012. Degradation of permafrost beneath a road embankment enhanced by heat advected in groundwater 1. Can. J. Earth Sci. 49, 953–962. https://doi.org/10.1139/E2012-018.

Denicol, P.S., Jing, X.D., 1998. Effects of water salinity, saturation and clay content on the complex resistivity of sandstone samples. Geol. Soc. Spec. Publ. 136, 147–157. https://doi.org/10.1144/GSL.SP.1998.136.01.13.

Doetsch, J., Ingeman-Nielsen, T., Christiansen, A.V., Fiandaca, G., Auken, E., Elberling, B., 2015. Direct current (DC) resistivity and induced polarization (IP) monitoring of active layer dynamics at high temporal resolution. Cold Reg. Sci. Technol. 119, 16–28. https://doi.org/10.1016/j.coldregions.2015.07.002.

Doyoro, Y.G., Chang, P.-Y., Puntu, J.M., 2021. Uncertainty of the 2D Resistivity Survey on the Subsurface Cavities. Appl. Sci. 11, 3143. https://doi.org/10.3390/app11073143.

Ebiegberi, O., Isaac Oludayo, A., 2021. Effect of grain size distribution on field resistivity values of unconsolidated sediments quest journals. J. Res. Environm. Earth Sci. 7 (1), 12–18.

Elverhøi, Anders, Svendsen, John Inge, Solheim, Anders, Andersen, Espen Sletten, Milliman, John, Mangerud, Jan, Hooke, Roger LeB, 1995. Age determination of sediments off western Svalbard. PANGAEA, doi:10.1594/PANGAEA.707941, Supplement to: Elverhoi, A et al. (1995): late Quaternary sediment yield from high Arctic Svalbard area. J. Geol. 103, 1–17. https://doi.org/10.1086/629718.

Erchul, R.A., 1972. The Use of Electrical Resistivity to Determine Porosity of Marine Sediemnts. University of Rhode Island. PhD thesis.

Fiandaca, G., Auken, E., Christiansen, A.V., Gazoty, A., 2012. Time-domain-induced polarization: Full-decay forward modeling and 1D laterally constrained inversion of Cole-Cole parameters. Geophysics 77. https://doi.org/10.1190/geo2011-0217.1.

Fortier, R., Allard, M., Seguin, M.K., 1994. Effect of physical properties of frozen ground on electrical resistivity logging. Cold Reg. Sci. Technol. 22, 361–384. https://doi.org/10.1016/0165-232X(94)90021-3.

Forwick, M., Vorren, T.O., 2009. Late weichselian and holocene sedimentary environments and ice rafting in Isfjorden, Spitsbergen. Palaeogeogr. Palaeoclimatol. Palaeoecol. 280, 258–274. https://doi.org/10.1016/j.palaeo.2009.06.026.

Fukue, M., Minato, T., Horibe, H., Taya, N., 1999. The micro-structures of clay given by resistivity measurements. Eng. Geol. 54, 43–53. https://doi.org/10.1016/S0013-7952(99)00060-5.

Gilbert, G.L., O'Neill, H.B., Nemec, W., Thiel, C., Christiansen, H.H., Buylaert, J.P., 2018. Late Quaternary sedimentation and permafrost development in a Svalbard fjord-valley, Norwegian high Arctic. Sedimentology 65, 2531–2558. https://doi.org/10.1111/sed.12476.

Gilbert, G.L., Instanes, A., Sinitsyn, A.O., Aalberg, A., 2019. Characterization of two sites for geotechnical testing in permafrost: Longyearbyen, Svalbard. AIMS Geosci. 5 (4), 868–885. https://doi.org/10.3934/geosci.2019.4.868.

Hanssen-Bauer, E.J., Førland, H., Hisdal, S., Mayer, A.B., Sandø, Sorteberg, A., 2019. Climate in Svalbard 2100. NCCS report 1/2019.

Hauck, C., 2002. Frozen ground monitoring using DC resistivity tomography. Geophys. Res. Lett. 29, 12–1-NaN-12–4. https://doi.org/10.1029/2002GL014995.

Hauck, C., Bach, M., Hilbich, C., 2008. A four-phase model to quantify subsurface ice and water content in permafrost regions based on geophysical data sets. In: Proc. 9th Int. Conf. Permafr, pp. 675–680.

Hellman, K., Johansson, S.J., Olsson, P.O., Dahlin, T.D., 2016. Resistivity inversion software comparison. In: 22nd Eur. Meet. Environ. Eng. Geophys. Near Surf. Geosci. 2016. https://doi.org/10.3997/2214-4609.201602016.

Hornum, M.T., Betlem, P., Hodson, A., 2021. Groundwater flow through continuous permafrost along geological boundary revealed by electrical resistivity tomography. Geophys. Res. Lett. 48, e2021GL092757.

Ingólfsson, Ólafur, Landvik, J.Y., 2013. The svalbard-barents sea ice-sheet-historical, current and future perspectives. Quat. Sci. Rev. https://doi.org/10.1016/j.quascirev.2012.11.034.

Keating, K., Binley, A., Bense, V., Van Dam, R.L., Christiansen, H.H., 2018. Combined geophysical measurements provide evidence for unfrozen water in permafrost in the adventdalen valley in Svalbard. Geophys. Res. Lett. 45, 7606–7614. https://doi.org/10.1029/2017GL076508.

King, M.S., Zimmerman, R.W., Corwin, R.F., 1988. Seismic and electrical properties of unconsolidated permafrost. Geophys. Prospect. 36 (4), 349–364.

Landvik, J.Y., Bondevik, S., Elverhøi, A., Fjeldskaar, W., Mangerud, J., Salvigsen, O., Siegert, M.J., Svendsen, J.I., Vorren, T.O., 1998. The last glacial maximum of Svalbard and the barents sea area: ice sheet extent and configuration. Quat. Sci. Rev. 17, 43–75. https://doi.org/10.1016/S0277-3791(97)00066-8.

Landvik, J.Y., Ingólfsson, Ó., Mienert, J., Lehman, S.J., Solheim, A., Elverhøi, A., Ottesen, D., 2005. Rethinking late Weichselian ice-sheet dynamics in coastal NW Svalbard. Boreas 34, 7–24. https://doi.org/10.1080/03009480510012809.

Lemke, P., Ren, J., Alley, R.B., Allison, I., Carrasco, J., Flato, G., Fujii, Y., Kaser, G., Mote, P., Thomas, R.H., Zhang, T., 2007. Observations: Changes in snow, ice and frozen ground. In: Solomon, S., Qin, D., Manning, M., Chen, Z., Marquis, M., Averyt, K.B., Tignor, M., Miller, H.L. (Eds.), Climate Change 2007: The Physical Science Basis. Contribution of Working Group I to the Fourth Assessment Report of the Intergovernmental Panel on Climate Change. Cambridge University Press, Cambridge, United Kingdom and New York, NY, USA.

Lesmes, D.P., Frye, K.M., 2001. Influence of pore fluid chemistry on the complex conductivity and induced polarization responses of Berea sandstone. J. Geophys. Res. Solid Earth 106, 4079–4090. https://doi.org/10.1029/2000jb900392.

Loke, D.M.H., 2011. 2-D and 3-D electrical imaging surveys. Tutorial 122.

Lønne, I., 2005. Faint traces of high Arctic glaciations: an early Holocene ice-front fluctuation in Bolterdalen, Svalbard. Boreas 34, 308–323. https://doi.org/10.1111/j.1502-3885.2005.tb01103.x.

Lønne, I., Lyså, A., 2005. Deglaciation dynamics following the little ice age on Svalbard: implications for shaping of landscapes at high latitudes. Geomorphology. 72, 300–319. https://doi.org/10.1016/j.geomorph.2005.06.003.

Lønne, I., Nemec, W., 2004. High-arctic fan delta recording deglaciation and environment disequilibrium. Sedimentology 51, 553–589. https://doi.org/10.1111/j.1365-3091.2004.00636.x.

Lu, Y., Abuel-Naga, H., Al Rashid, Q., Hasan, M.F., 2019. Effect of pore-water salinity on the electrical resistivity of partially saturated compacted clay liners. Adv. Mater. Sci. Eng. 2019 https://doi.org/10.1155/2019/7974152.

Major, H., Haremo, P., Dallmann, W.K., Andresen, A., 2001. Geological Map of Svalbard 1, 100,000, Norsk Polarinst, Map C9G Adventdalen, pp. 31–32.

Mangerud, J., Dokken, T., Hebbeln, D., Heggen, B., Ingólfsson, Ó., Landvik, J.Y., Mejdahl, V., Svendsen, J.I., Vorren, T.O., 1998. Fluctuations of the svalbard-barents sea ice sheet during the last 150000 years. Quat. Sci. Rev. 17, 11–42. https://doi.org/10.1016/S0277-3791(97)00069-3.

Mcbean, G., Alekseev, G., Chen, D., Førland, E., Fyfe, J., Groisman, P.Y.P., King, R., Melling, H., Vose, R., Whitfield, P.P.H., 2005. Arctic climate: past and present. In: Arct. Clim. Impact Assessment. Cambridge Univ. Press, Cambridge, UK, pp. 21–60.

Muñoz-Castelblanco, J.A., Pereira, J.M., Delage, P., Cui, Y.J., 2012. The influence of changes in water content on the electrical resistivity of a natural unsaturated loess. Geotech. Test. J. 35 https://doi.org/10.1520/GTJ103587.

Oldenborger, G.A., LeBlanc, A.M., 2015. Geophysical characterization of permafrost terrain at Iqaluit International Airport. Nunavut. J. Appl. Geophys. 123, 36–49. https://doi.org/10.1016/j.jappgeo.2015.09.016.

Parasnis, D.S., 1979. Principles of Applied Geophysics, 1st ed. Springer Netherlands. https://doi.org/10.1007/978-94-009-5814-2.

Slater, L.D., Lesmes, D., 2002. IP interpretation in environmental investigations. Geophysics 67, 77–88. https://doi.org/10.1190/1.1451353.

Svendsen, J.I., Mangerud, J., 1997. Holocene glacial and climatic variations on Spitsbergen, Svalbard. Holocene 7, 45–57. https://doi.org/10.1177/095968369700700105.

Takakura, S., 2009. Influence of pore-water salinity and temperature on resistivity of clay-bearing rocks. BUTSURI-TANSA (Geophysical Explor.) 62, 385–396. https://doi.org/10.3124/segj.62.385.

Tavakoli, S., Elming, S.Å., Thunehed, H., 2012. Geophysical modelling of the central Skellefte district, Northern Sweden; an integrated model based on the electrical, potential field and petrophysical data. J. Appl. Geophys. 82, 84–100. https://doi.org/10.1016/j.jappgeo.2012.02.006.

Tavakoli, S., Bauer, T.E., Rasmussen, T.M., Weihed, P., Elming, S.Å., 2016a. Deep massive sulphide exploration using 2D and 3D geoelectrical and induced polarization data in Skellefte mining district, northern Sweden. Geophys. Prospect. 64, 1602–1619. https://doi.org/10.1111/1365-2478.12363.

Tavakoli, S., Dehghannejad, M., de los Ángeles García Juanatey, M., Bauer, T., Weihed, P., Elming, S.-Å., 2016b. Potential field, geoelectrical and reflection seismic investigations for massive sulphide exploration in the Skellefte mining district, Northern Sweden. Acta Geophys. 64, 2171–2199.

Tavakoli, S., Sarlus, Z., Kronsell, I., Bauer, T.E., 2021. 2.5D geophysical model of the Gällivare mining area: an integrated study to model the top 4 km of the subsurface and guide for future exploration activities. Geophys. Prospect. 69, 821–841. https://doi.org/10.1111/1365-2478.13077.

Watanabe, T., Matsuoka, N., Christiansen, H.H., 2012. Mudboil and ice-wedge dynamics investigated by electrical resistivity tomography, ground temperatures and surface movements in Svalbard. Geogr. Ann. Ser. A Phys. Geogr. 94, 445–457. https://doi.org/10.1111/j.1468-0459.2012.00470.x.